Increase in elastic and hardness anisotropy of titanium with oxygen uptake due to high temperature oxidation: A multimodal framework using high speed nanoindentation mapping

Damien Texier, Thiebaud Richeton, Henry Proudhon, Ayyoub Dziri, Quentin Sirvin, Marc Legros

Increase in elastic and hardness anisotropy of titanium with oxygen uptake due to high temperature oxidation: A multimodal framework using high speed nanoindentation mapping

Damien Texier[a], Thiebaud Richeton[b], Henry Proudhon[c], Ayyoub Dziri[a], Quentin Sirvin[a], Marc Legros[d]

[a]*Institut Clement Ader (ICA) - UMR CNRS 5312, Université de Toulouse, CNRS, INSA, UPS, Mines Albi, ISAE-SUPAERO, Campus Jarlard, 81013 Albi Cedex 09, France*
[b]*Université de Lorraine, CNRS, Arts et Métiers, LEM3, F-57000 Metz, France*
[c]*MINES Paris, PSL University, MAT - Centre des matériaux, CNRS UMR 7633, BP 87, 91003 Evry, France*
[d]*CEMES, 29 rue Jeanne Marvig; Toulouse, France*

Abstract

Titanium and its alloys combine an important mechanical anisotropy and a high capacity to dissolve oxygen. The detailed evolution of the elastic compliance of titanium as a function of its oxygen content is only partially known, despite its importance in structural applications. Here, high speed nanoindentation mapping (HSNM) was conducted on a grade 2 commercially pure titanium (CP-Ti) to probe elastic and hardness anisotropy as well as property evolution as a function of the oxygen content within Ti using pre-oxidized specimens. The oxygen concentration investigated ranged from 600 ppm to 20 % atomic. Pre-oxidation of the CP-Ti was performed at 700 °C for 100 h under air to create a gradient of oxygen content within the metal, denoted oxygen-rich layer (ORL). Local oxygen content was quantified using microprobe analyses (EPMA) and crystal orientation using electron backscattered diffraction (EBSD). Reduced modulus and hardness maps were obtained on the pre-oxidized sample within the ORL and far from the ORL using large but highly resolved nanoindentation technique in continuous stiffness measurement (CSM) mode. Data merging techniques were used on this multi-modal dataset to statistically link local mechanical properties to chemical and crystal orientation information. Oxygen insertion in the Ti lattice was found to significantly increase the hardness and elastic moduli of titanium and was correlated to orientation of the c-axis of the α-Ti as a function of the nanoindentation loading direction. Using the Vlassak and Nix theory, it was possible to identify the evolution of the C_{ij} terms of the stiffness matrix as a function of the oxygen content up to 20 % at. in O.

Keywords: Titanium, Oxygen strengthening, Nanoindentation, Elastic anisotropy, Hardness anisotropy.

1. Introduction

Titanium and titanium alloys are widely used as lightweight materials in industry due to high specific strength at room and intermediate temperatures [1]. The motivation to substitute iron-based and nickel-based alloys by titanium

*Corresponding author
Email address: damien.texier@mines-albi.fr (Damien Texier)

alloys for structural components used at intermediate temperature is altered by the high solubility of oxygen in titanium within both the α-Ti and β-Ti phases [2]. Titanium and its alloys, exposed at intermediate temperature under oxidizing environment, form an external oxide scale but also an oxygen-rich layer (ORL) beneath the external oxide due to high oxygen solubility and diffusion within titanium [3]. The ORL extends particularly deep beneath the external oxide scale compared to the growth of the latter, nearly one order of magnitude higher depending on the material and temperature [4–6]. The ORL demonstrates a brittle behavior, leading to premature cracking under tensile loading [3, 7–27]. Such early cracking is highly detrimental for the mechanical integrity of thin components, as recently reported in Refs. [21, 23, 27]. In addition, oxygen embrittlement and early cracking of the ORL subjected to thermomechanical stresses were found to strongly impair the fatigue endurance and lifetime of oxidized titanium [7, 14, 17–19, 24]. Therefore, assessing local mechanical properties and deformation mechanisms within the ORL is of high interest to better predict strain/stress distribution within the ORL and early damage development at the microstructure scale.

The effect of oxygen insertion in titanium on its mechanical properties has been extensively studied in the literature. Oxygen addition even at low concentration (thousands of ppm of oxygen, *i.e.*, fractions of atomic percent of oxygen) can significantly improve the tensile strength of titanium [9, 15, 26, 28–31] at the expense of the ductility [3, 9, 16, 26, 31]. Furthermore, oxygen increases hardness of titanium even for slight change in O concentration [3, 6, 8, 10–12, 17–19, 25, 30–35]. Such characterizations were conducted on either bulk samples with homogeneous but low oxygen content (around 1.5 % atomic maximum [34]) or pre-oxidized titanium samples to cover a large range of oxygen concentrations. For the latter case, the oxygen concentration can range from hundreds of ppm (bulk concentration) to 25-30 % atomic at the metal/oxide interface [6, 8, 11, 12, 17, 27, 35]. Oxidation then diffusion techniques on thin foils also aimed at probing the mechanical properties of oxygen-rich titanium up to 20 % at. with a homogeneous concentration in the bulk [12, 36]. Correlative analyses between hardness measurements and oxygen profiles aimed to identify different models, either linear [11, 19, 37], parabolic [3, 6, 27] or following a power law form [8, 12, 33] to link hardness properties to the oxygen content. At an oxygen concentration of 25 % at., hardness of titanium is about 2.7 to 2.9 times higher for Ti6242S [6, 19], 1.8 to 2.4 times higher for Ti64 [11, 27], and 6.7 times higher for grade 1 Commercially Pure titanium (CP-Ti) [33]. In addition, hardness properties of titanium were also found to be highly sensitive to the crystallographic orientation, regardless of the oxygen content. Indeed, hardness measurements performed along directions in the basal plane are 40 to 70 % softer than the measurements along the *c*-axis direction [33, 35, 38–45]. Using multi-modal map correlation techniques, Maggazeni et al. [33] also proposed a power law and sinusoidal evolution of the hardness as a function of the oxygen content and declination angle between the *c*-axis direction and the indentation direction, respectively. These changes in hardness properties are related to the variation of slip and twinning activities as a function of the crystal orientation but also the oxygen concentration [3, 7, 9, 10, 13, 15, 20, 23, 25, 28, 30, 46].

While change in hardness properties were particularly investigated, a few studies documented either elastic anisotropy [33, 35, 39–45] or average stiffness evolutions of titanium with different oxygen contents [10, 15, 27, 30, 34, 35, 46–48], but not the combination of both the factors. Terms of the stiffness matrix for CP-Ti, defining its

elastic anisotropy, were established in the literature and summarized in Table 4 in **Appendix 1**. Different sets of C_{ij} parameters were found, but those used or identified in Refs. [42, 49–55] will be considered here due to similarities. Weaver et al. [42] performed finite element calculations to simulate the indentation modulus according to different declination angles, thus probing both the multiaxial loading of indentation tips (a Berkovich tip in this case) and the crystal elastic anisotropy. Good agreement between numerical simulations and experimental measurements aimed at validating such an approach to identify C_{ij} terms from nanoindentation. As far as the evolution of the elastic modulus with the oxygen content is concerned, some identifications were done in the literature for low oxygen alloyed titanium or oxygen-graded titanium [10, 15, 27, 30, 34, 35, 46–48]. Lee et al. [46] established a linear increase of the isotropic Young's modulus of 4 to 5 GPa for each atomic percent of oxygen at low oxygen content. At higher oxygen concentration, the Young's modulus of the Ti64 alloy was found to increase of 2.3 per atomic percent of oxygen with two regimes around 0.5 % at. in O [27]. To the best of the authors' knowledge, the evolution of the stiffness matrix for CP-titanium and titanium alloys as a function of the oxygen concentration was not documented in the literature, except using atomic simulations (see Table 5 in **Appendix 1** from Liang [56]). However, assessment of the stiffness matrix for different oxygen contents is of high importance for further (i) evaluation of stress/strain concentration in polycrystalline aggregates of CP-Ti subjected to high temperature oxidation and (ii) clarification of the role of crystallographic configurations favoring oxygen embrittlement for structural applications.

The present study intends to investigate both the hardness and elastic response of CP-titanium with different concentrations of oxygen. New developments in high speed nanoindentation mapping (HSNM) [33, 45, 57–59] and multi-modal correlative microscopy [33, 35, 38, 39, 41, 42, 45, 58, 60] will be used to correlate indentation properties to the oxygen content and crystal orientation. For comparison with the existing literature, the multi-modal analysis was first applied to bulk CP-Ti, *i.e.*, to document both the elastic and hardness anisotropy without contribution of oxygen. Then, a one-direction analysis was conducted to evaluate changes in elastic and hardness properties as a function of the oxygen content, regardless of the crystallographic orientation. Finally, the multi-modal correlative microscopy using HSNM in continuous stiffness measurement (CSM) mode [61], electron backscaterred diffraction (EBSD) and microprobe analyses (EPMA) will be applied to a pre-oxidized CP-titanium material to locally probe the mechanical response of titanium with up to 20 % at. oxygen dissolved. Semi-analytical solutions based on the Vlassak and Nix theory [62, 63] will be used to approximate the indentation modulus for materials with an anisotropic elastic behavior and subsequently identify the evolution of the C_{ij} terms as a function of the oxygen concentration. The latter material characterization constitutes the originality of the present work and will be of interest for further mechanical simulations of polycrystalline aggregates. Both experimental and simulated results will be discussed.

2. Material and experiments

2.1. Material and specimen preparation

The material studied is a grade 2 commercially pure titanium (CP-Ti) provided by All Metal Services in the form of a 1.8 mm-thick sheet. Its nominal composition, characterized by Nippon Steel Corporation, is reported in Table 1. The material has an α-phase equiaxe grains microstructure with some iron silicides and β-grains located at grain boundaries. The average grain size in the as-received state is of 15±5 μm.

Rectangular specimens with dimensions of 10×5×1.8 mm^3 were extracted from the plate using an IsoMet High Speed precision cutter from Buehler. Specimen surfaces were ground down to P4000 SiC paper using a precision jig to ensure a good control of the sample parallelism [64]. The specimen was cleaned in acetone then ethanol for 15 min using ultrasonic bath before high temperature treatment or oxidation to induce oxygen ingress within titanium. A thermal treatment of 700 °C-100 h, *i.e.*, a pre-oxidation treatment, was performed using a Nabertherm C290 furnace with static atmosphere (no air stirring) to trigger both grain growth and oxygen diffusion from the surface. The sample was introduced at high temperature and positioned onto an alumina plate, its side of interest facing the air. To select the best material plane for further nanoindentation tests, the heat-treated microstructure of the bulk material was characterized using electron backscattered diffraction (EBSD) technique. EBSD maps in relation to the different process directions, *i.e.*, the rolling direction (RD), the long transverse direction (LTD), and the short transverse direction (STD) corresponding to the specimen thickness direction, are illustrated in Fig. 2(a-c). The grain size of the heat treated CP-Ti material was measured to 88 μm. The EBSD orientation map in reference to LTD presents various grain orientations, as confirmed by the homogeneous orientation distribution function represented in the inverse pole figure (Fig. 2(f)). EBSD data were also post-treated to represent the angle between the process directions and the c-axis of the α-Ti lattice, the so-called declination angle, $\%$, as illustrated in Fig. 2(g-i). The distribution function of the declination angle was also depicted in Fig. 2(j-l). These preliminary characterizations aimed at selecting the plane normal to LTD to be tested using nanoindentation to probe the largest variety of grain orientations. For information, a schematic illustration of the cross-section of the pre-oxidized specimen showing the external oxide scale, the ORL and the two regions of interest for the nanoindentation mapping is depicted in Fig. 1: (i) the bulk specimen far from the ORL and (ii) the pre-oxidized specimen in the ORL.

Table 1: Nominal composition of the grade 2 CP-Ti material used in this study (in weight %

Ti	O	Fe	N	C	H
Bal.	0.14	0.07	<0.005	<0.005	0.0007

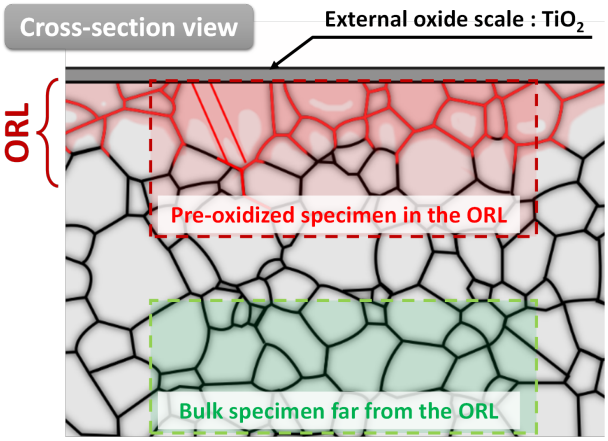

Figure 1: Schematic illustration of the cross-section of the pre-oxidized specimen showing the external oxide scale, the ORL and the different regions of interest for the nanoindentation mapping.

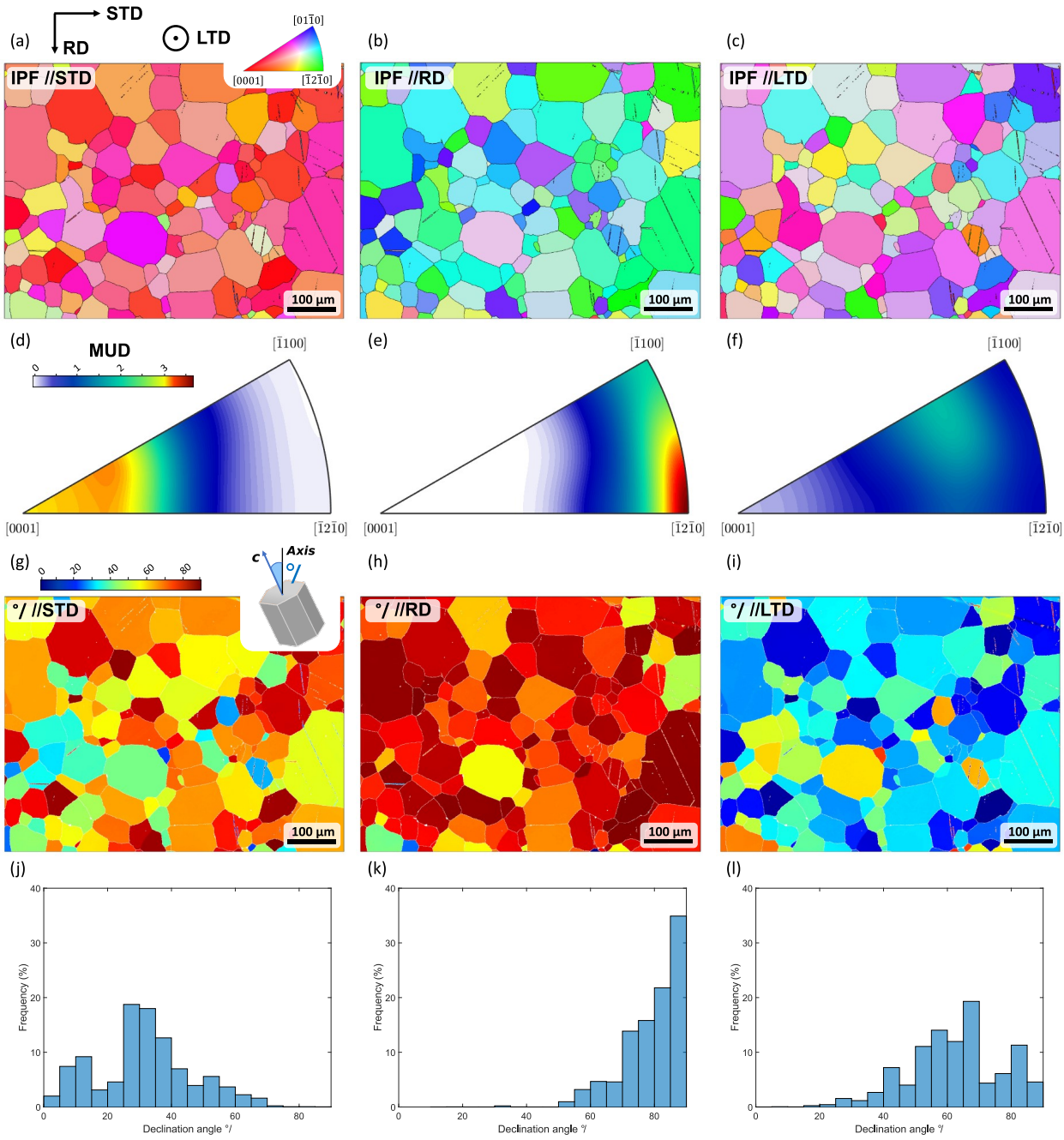

Figure 2: Texture characterization of the CP-Ti after heat-treatment for selection of the plane to be tested by nanoindentation according to the different process directions, *i.e.*, STD, RD, LTD. (a-c) EBSD orientation maps, (d-f) Orientation distribution function represented on an IPF with a maximal multiple of uniform density of 3.7, (g-i) Declination angle map (°/), (j-l) Distribution function of the declination angle.

For convenience, specimens for oxidation were prepared so that the oxygen ingress is along STD and the cross-section plane for nanoindentation testing is the STD-RD plane. After oxidation, the specimen was mounted in a low shrinkage cold epoxy resin. The mounted specimen was polished down to a 1 μm diamond paste finish. This surface

finish was used for microprobe analyses (EPMA) prior to electron backscattered diffraction (EBSD) characterization and nanoindentation testing. After EPMA characterization, a mechanochemical polishing using colloidal silica during 40 min was applied to the sample for further EBSD and nanoindentation testing. The specimen was then abundantly washed then swiped using water. The specimen was cleaned in ethanol for 15 min using ultrasonic bath.

2.2. Characterization techniques

Observations were conducted using a JEOL JSM 7100F scanning electron microscope. EBSD maps were acquired at 20 keV with a step size of 0.5 μm with a CMOS Symmetry S2 EBSD detector (Oxford Instruments) after nanoindentation. EBSD data were post-treated and plotted using MTex [65] and the open source Pymicro library[1] [66] for further correlative multi-modal microscopy.

EPMA characterization was performed to characterize the oxygen ingress and concentration within the oxygen-rich layer (ORL) down to the specimen core. A particular attention was paid to the specimen preparation to limit edge blunting and the formation of the native TiO_2. It is important to better assess oxygen content in the vicinity of the metal/oxide interface [5]. The sample was coated with a thin carbon layer then stored in a vacuum chamber (10^{-5} *mbar*) before EPMA analyses. EPMA measurements were performed using a CAMECA© SXFive FE at an acceleration voltage of 10 kV and a probe current of 20 nA. Calibration of elements were used for quantitative analyses. The absolute error on the oxygen content is close to 0.2 atomic percent. Four profiles were performed to document the oxygen profile in the ORL with a step size of 1 μm near the surface (first 25 μm beneath the oxidized surface) and of 3 μm in the bulk. Due to passivation of titanium at room temperature, the oxygen content was measured relative to a reference state, *i.e.*, the non-oxidation affected material, by spectrum substraction of the oxygen spectrum (5 measurements in the bulk). The spectrum intensity corresponding to the oxygen was then deducted from the spectrum for each EPMA measurement. Therefore, the oxygen content presented in the paper does not correspond to the absolute oxygen content, but the oxygen uptake due to oxygen dissolution during oxidation, and is denoted Δ[O].

2.3. Nanoindentation tests

High speed nanoindentation mapping (HSNM), also called in the literature as "High throughput nanoindentation" or "mechanical microscopy mapping", was performed using a NMT04 *in-situ* nanoindentation system from Femtotools^{AG} in continuous stiffness measurement (CSM) mode under displacement control (See **Appendix 2** for additional details on the CSM measurements and illustrations in Fig. 13). Measurement under displacement-controlled mode is important for such experiments, based on the high difference in hardness and elastic properties expected for the oxygen-graded material. This actuation technique aims to maintain similar indentation depths from indent to indent, regardless of the local mechanical response. This allows to maintain similar interaction volumes between the indenter tip and the sample throughout the testing area in order to quantify variations in properties in a consistent

[1] `https://github.com/heprom/pymicro`

way. On the contrary, force-controlled nanoindentation can lead to widely different indentation depths and inconsistent measurements of local materials properties based on different interaction volumes and sensitivity to measurement artifacts such as indentation size effect.

The nanoindentation system was equipped with a diamond Berkovich tip and a 20 mN load cell with a position noise floor of ±0.05 nm and a load noise of ±0.05 μN (MEMS sensor). The reference stiffness of the nanoindentation system was of 11468.8 kN.mm^{-1} (This includes the stiffness of the force sensing elements). Displacement, load, position, phase shift are measurement at a frequency f_{test} of 94 kHz but analyzed for calculation of the reduced modulus E_R and hardness H at a frequency $f_{acquis.}$ of 50 to 400 Hz, the CSM frequency f_{CSM} being of 200 Hz in the present investigation. The calibration of the diamond Berkovich tip was done on fused silica using the CSM technique in displacement-controlled mode and stable values of E_R and H for the fused silica ranged from 20 to 160 nm (See **Appendix 2** for additional details on the Berkovich tip calibration and Fig. 14 for the calibration curves).

Three nanoindentation maps were conducted to probe the effect of the crystal orientation and oxygen ingress on the nanoindentation response. The nanoindentation parameters for each nanoindentation map are reported in Table 2.

2.4. Nanoindentation model for correlative microscopy

Considering linear viscoelasticity, Sneddon's stiffness equation can be used to relate the dynamic stiffness and damping of the contact to the elastic modulus, *E'*, and the loss modulus, *E"* [61, 67]:

$$\frac{E'}{1-\nu^2} = \frac{\Delta F}{\Delta h} cos(\phi) \frac{\sqrt{\pi}}{2\beta\sqrt{A}} \tag{1}$$

and

$$\frac{E''}{1-\nu^2} = \frac{\Delta F}{\Delta h} sin(\phi) \frac{\sqrt{\pi}}{2\beta\sqrt{A}} \tag{2}$$

with ν the Poisson's ratio of the tested material, ΔF the load amplitude, Δh the displacement amplitude, ϕ the phase shift, β a tip shape descriptor (β = 1.034 for a Berkovich tip [68]), and A the projected contact area.

Table 2: Nanoindentation parameters in CSM mode and displacement control mode

	Bulk-Ti	O-graded Ti (large)	O-graded Ti (HR)
Array size (indents)	400 × 150	1100 × 100	470 × 190
Step size (μm)	2.5	2.5	0.8
Max depth (nm)	180	180	50
Load rate (nm.s^{-1})	120	120	25
CSM frequency (Hz)	200	200	200
Displacement amplitude (nm)	5	5	5

The reduced modulus E_R can be expressed as a function of the elastic modulus E', the indentation modulus E_{Ind}, the Young's modulus of the diamond $E_{Diamond}$ and its Poisson's ratio $\nu_{Diamond}$:

$$\frac{1}{E_R} = \frac{1-\nu^2}{E'} = \frac{1}{E_{Ind}} + \frac{1-\nu_{Diamond}^2}{E_{Diamond}} \tag{3}$$

Vlassak and Nix theory [62, 63, 69] is capable to theoretically evaluate E_{Ind} for a given crystal orientation using surface Green's function [70]. Assuming that the indenter geometry corresponds to a circular flat punch, Vlassak and Nix have shown that E_{Ind} can be computed as:

$$E_{Ind} = \frac{4\pi}{\int_0^{2\pi} n_i B_{ij}^{-1}(\omega) n_j \, d\omega} \tag{4}$$

where $\boldsymbol{n}$ is the unit normal to the indentation surface in the crystal's coordinates. The symmetric matrix $\boldsymbol{B}$ was originally expressed as a line integral within the Stroh integral formalism [62, 63, 69]. However, it is computed more efficiently using the Stroh matrix (or sextic) formalism (see, e.g., Refs. [71–74]) which needs first to solve an eigenvalue problem:

$$\boldsymbol{N}\boldsymbol{\xi}^{\alpha} = p_{\alpha}\boldsymbol{\xi}^{\alpha} \tag{5}$$

where $\boldsymbol{N}$ is a 6×6 matrix given by:

$$\boldsymbol{N} = -\begin{pmatrix} (\boldsymbol{nn})^{-1}(\boldsymbol{nm}) & (\boldsymbol{nn})^{-1} \\ (\boldsymbol{mn})(\boldsymbol{nn})^{-1}(\boldsymbol{nm}) - (\boldsymbol{mm}) & (\boldsymbol{mn})^{-1}(\boldsymbol{nn})^{-1} \end{pmatrix} \tag{6}$$

$\boldsymbol{N}$ is related to the anisotropic elastic stiffness tensor $\boldsymbol{C}$ according to the notation $(mn)_{jk} = m_i C_{ijkl} n_l$. $\boldsymbol{m} = \boldsymbol{n} \wedge \boldsymbol{t}$ where $\boldsymbol{t}$ is an arbitrary unit vector in the plane perpendicular to $\boldsymbol{n}$. It makes an angle ω with a fixed datum of the plane perpendicular to $\boldsymbol{n}$. ω corresponds to the angle that varies from 0 to 2π in the line integral of Eq. 4. Then, p_α are the six eigenvalues of the matrix $\boldsymbol{N}$. These eigenvalues always appear in the form of 3 pairs of complex conjugates [71–74]. By convention, $p_{i+3} = \overline{p}_i$ and $\mathrm{Im}(p_i) > 0$ for $i = 1$ to 3. $\boldsymbol{\xi}^{\alpha}$ are the eigenvectors that are split into two 3×1 column vectors as:

$$\boldsymbol{\xi}^{\alpha} = \begin{pmatrix} \boldsymbol{A}^{\alpha} \\ \boldsymbol{L}^{\alpha} \end{pmatrix} \tag{7}$$

$\boldsymbol{A}^{\alpha}$ and $\boldsymbol{L}^{\alpha}$ are normalized according to the relation:

$$\sum_{i=1}^{3} A_i^{\alpha} L_i^{\beta} + A_i^{\beta} L_i^{\alpha} = \delta_{\alpha\beta} \tag{8}$$

Finally, the matrix $\boldsymbol{B}$ is obtained as:

$$B_{ij} = 2\mathrm{i} \sum_{\alpha=1}^{3} L_i^{\alpha} L_j^{\alpha} \tag{9}$$

A Gauss-Legendre quadrature method is used to solve the line integral of Eq. 4. An accuracy of 10^{-4} % is reached with 30 integration points. In combination with the use of the matrix formalism, this result is very short computation times to get E_{Ind} (<< 1s). The above theoretical framework is rigorously valid for a circular contact area. For an indenter with a triangular shape like a Berkovich, the indentation modulus E_{Ind} depends on the orientation of the indenter in the indentation surface. Vlassak and Nix [62] have shown that these variations are very small and can be reasonably neglected considering the experimental scatter. However, they have also shown that the indentation moduli for triangular indenter are on average 6 % higher that the corresponding moduli for axysymmetric indenter [62]. Hence, a corrective multiplicative factor of 1.06 is considered in this work to compute E_{Ind}, as was done by Aspinall et al. [75].

2.5. Multi-modal analyses

Three investigations were conducted to (1) investigate the role of crystallographic orientations on the nanoindentation response without contribution of the oxygen, (2) investigate the role of oxygen on the nanoindentation response independently of the local crystallographic orientation, (3) investigate both the role of oxygen content and crystallographic orientations on the nanoindentation response. The latter requires non-linear registrations in order to align data from different natures, *i.e.*, grain orientations from EBSD measurements and/or oxygen uptake from EPMA measurements, in the coordinate system of the nanoindentation maps. A quadratic registration model was applied using set of control points in the different modalities to correct for distortions in EBSD and EPMA fields. The net result is a multi-modal data set with EBSD maps, oxygen profiles and nanoindentation data that can be used for further analysis. For the correlative analysis, a Jupyter notebook was developed using Pymicro [66] to read EBSD and nanoindentation data, perform the registration and analyze the local material properties with respect to crystallographic orientation; the raw data and Python notebook are available publicly on [Zenodo] [76]. The Python code applying the Vlassak and Nix theory developed by Richeton and Berbenni is available at the following link [Github]. The representation of the spatial dependence of Young's modulus in 3D using the C_{ij} components of the stiffness tensor was done using a Python library developed by Kais AMMAR (*Centre des Matériaux, Mines Paris PSL*) [Github].

3. Results

3.1. Nanoindentation on the bulk material far from the ORL

HSNM was conducted on the heat-treated grade 2 CP-Ti material far from the oxygen diffusion zone to assess local mechanical properties, *i.e.*, hardness H and reduced modulus E_R, as a function of the grain orientation, without contribution of the oxygen content (see Fig. 3). This first investigation was conducted for validation of the multi-modal method based on the existing literature on such a characterization. As aforementioned, the specimen orientation was

purposely chosen to have a large panel of grain orientations to be tested using nanoindentation. EBSD maps were collected and the declination angle was calculated from EBSD data to only consider a scalar corresponding to the angle between the c-axis and the normal to the surface, *i.e.*, the indentation direction, as commonly used in the literature. E_R and H values ranged from 105 to 123 GPa and from 2.5 to 4.0 GPa, respectively. Both the reduced modulus and the hardness maps were capable to depict the anisotropic response of the material at the grain scale. It is worth mentioning that grains with stiff properties also experienced high hardness values, and correspond to grains with c-axis nearly parallel to the indentation direction (Fig. 3). Inversely, grains with c-axis nearly parallel to the surface plane are softer (lower reduced modulus and hardness).

Since, HSNM is capable to assess the anisotropic response of the material at the sub-grain level, combining HSNM and EBSD data aims to extract local mechanical properties as a function of the crystallographic orientation using multi-modal data merging techniques available in Pymicro. After data alignment, grains were segmented using a 5° misorientation threshold angle and a mask was computed from the grain boundary map to exclude HSNM data in the vicinity of grain boundaries (3 indents). Declination angles as well as position on inverse pole figure (IPF) were also calculated for each grain. The HSNM data were processed to consider the average reduced modulus and hardness per grain. Around 150 to 850 nanoindentation measurements were considered per grain, depending on the grain size. The hardness and the reduced modulus were then plotted as a function of the declination angle °/. As qualitatively observed, both the hardness (blue crosses) and the reduced modulus (red crosses) decreased with the declination angle, as shown in Fig. 4(a). Despite effort in plane selection for nanoindentation mapping, low declination angles were not tested here, most of the grains being inclined between 25 and 90 ° with the c-axis direction. For information, Magazzeni et al. [33] identified an evolution of the hardness as a function of the declination for CP-Ti material and this cos-form curve was added in Fig. 4(a) as a blue dashed curve. A good agreement is found between the present results and the identified hardness behavior from the literature. Similarly, Weaver et al. [42] identified the evolution of the indentation modulus as a function of the declination angle using finite element methods for a spherical indentation tip. Data were modified here to consider the reduced modulus corrected for a Berkovich diamond tip using Eq. 3 and a correction factor [75] (Red dotted curve in Fig. 4(a)). C_{ij} terms used for this model were taken from [42] and adapted from [50]. The modified Vlassak and Nix formulation was also used here using the same C_{ij} terms (Red dashed curve in Fig. 4(a)). Both models overestimate the present HSNM dataset, as for Weaver et al. [42]. Both the reduced modulus and the hardness were plotted on IPF maps, as depicted in Fig. 4(b) and (c). Grains mechanically tested along the [0001] direction have higher reduced modulus and hardness. Inversely, grains mechanically tested along the $[01\bar{1}0]$ and the $[\bar{1}2\bar{1}0]$ directions have the softest properties.

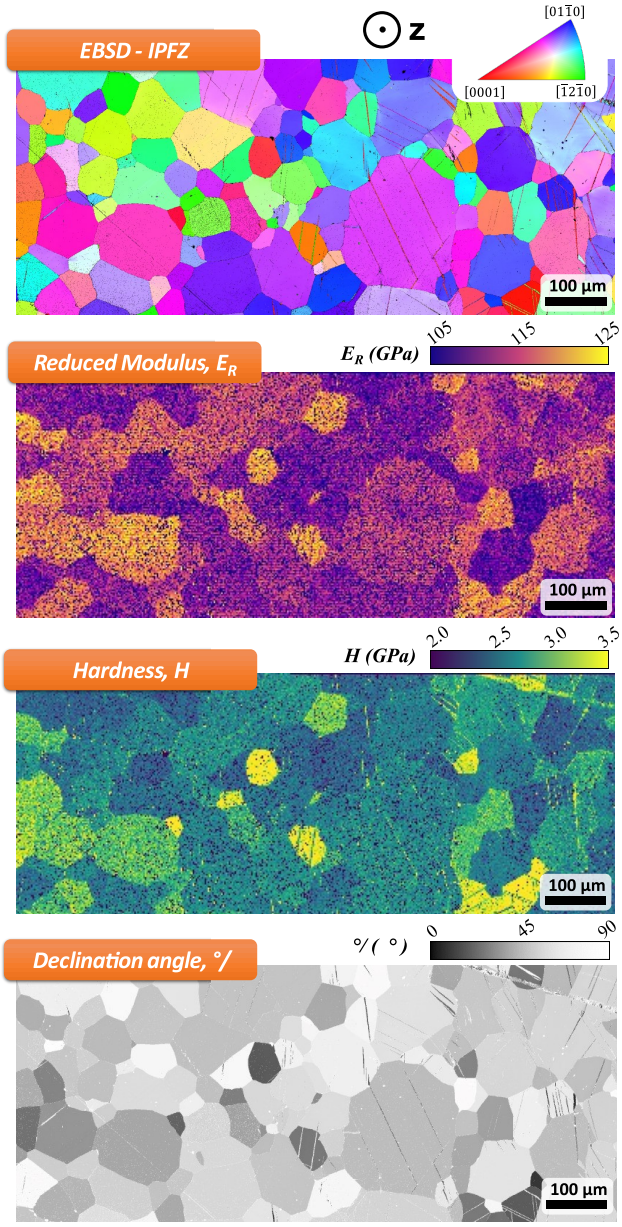

Figure 3: Grain orientation map in reference to the LTD/Z direction for the bulk CP-Ti material, Reduced modulus map using HSNM, Hardness map using HSNM, Declination (°/) map computed from EBSD measurements.

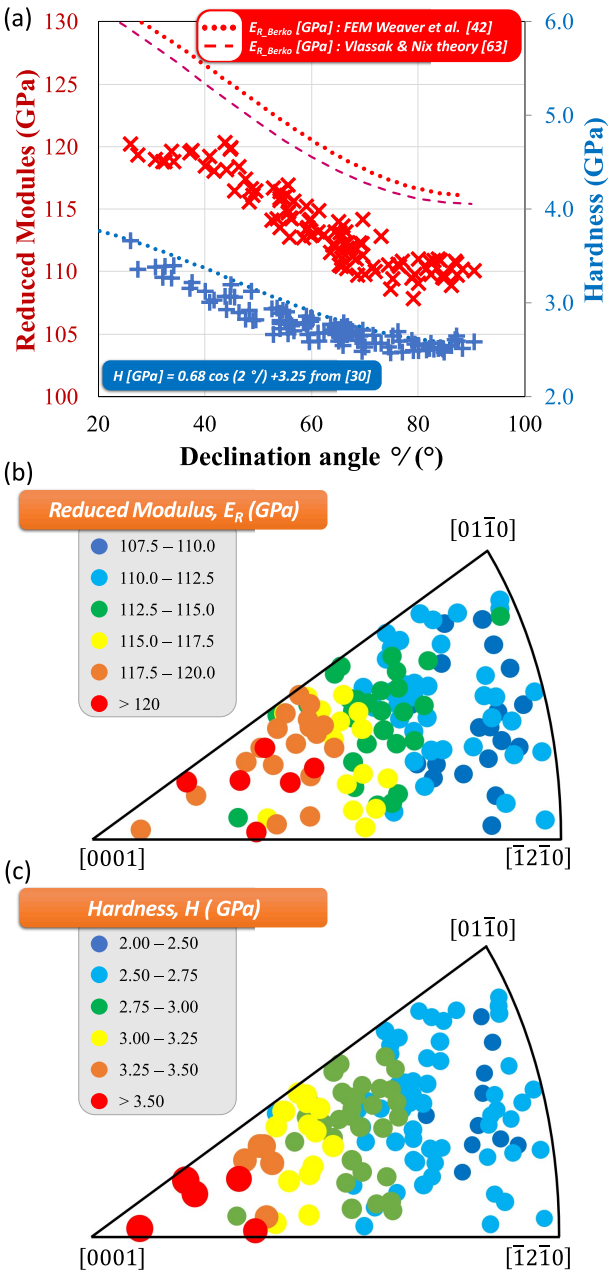

Figure 4: (a) Evolution of the reduced modulus and hardness as a function of the declination angle. Models [33, 42, 63] reported from the literature are added in the Figure for direct comparison. (b) Reduced modulus plotted in IPF standard triangle, and (c) Hardness plotted in IPF standard triangle.

3.2. Chemical and mechanical profile analyses of the oxygen rich layer (ORL)

CP-Ti was oxidized at 700 °C for 100 h so that the oxygen front is parallel to STD. Cross-sectional preparation was done to conduct chemical analyses and HSNM tests in the RD-STD plane. Four profiles of EPMA analyses were performed along STD to quantitatively measure the oxygen uptake within the ORL (Fig. 5(a)). In the ORL, the

oxygen content at the metal/oxide interface was nearly of 20 % at. and gradually decreases in depth. Oxygen profiles were fitted using an erf-type function derived from Fick's law in the case of the diffusion in a semi-infinite solid with a constant surface oxygen concentration $[O]_s$ and a diffusion coefficient D independent of the concentration and the position x [77]:

$$\frac{[O]_x - [O]_0}{[O]_s - [O]_0} = \frac{\Delta[O]_x}{\Delta[O]_{max}} = 1 - erf(\frac{x}{\sqrt{4Dt}}) \tag{10}$$

where $[O]_x$ is the oxygen concentration that diffuses at position x after a time t, $[O]_0$ is the oxygen concentration at the sample core. D and $\Delta[O]_{max}$ were identified (D = 5.5 $\cdot 10^{-16}$ $m^2.s^{-1}$ and $\Delta[O]_{max}$ = 25 % at.) to analytically relate the oxygen uptake as a function of the position from the metal/oxide interface, as depicted by a black dashed line in Fig. 5(a). The extension of the ORL was considered as the depth at an oxygen uptake of 0.5 % at.. The ORL extension was 45 μm for a 100 h oxidation at 700 °C.

HSNM was performed on this cross-section plane after surface preparation (map of 1100 × 100 indents). In a first approach, the average response of the hardness and reduced moduli was investigated, regardless of the crystallographic orientation to document the average relationship between H, E_R and $\Delta[O]$ using a power law function, similarly to Refs. [3, 6, 8, 12, 27, 33]. All the indents were positioned to the metal/oxide interface and the average properties over the 1100 profiles of indents was calculated. The average profiles of hardness and reduced modulus are plotted as a function of the distance from the metal/oxide interface in Fig. 5(b). A harder and stiffer behavior was found in the ORL compared to the bulk material far from the ORL, *i.e.*, the non-oxygen affected material. Hardness and reduced modulus gradually decreased with the penetration depth. This decrease in mechanical properties is particularly important down to 70 or even 100 μm deep for the reduced modulus and the hardness, respectively. Some property fluctuations can be observed after this depth, potentially due to crystallographic effects since the oxygen uptake is stabilized, as reported in the previous section for the nanoindentation response of bulk CP-Ti. The hardness and reduced modulus within the ORL at the metal/oxide interface are 5.3 and 1.3 times greater than the ones in the sample core. Knowing the oxygen uptake as a function of the metal/oxide interface, it is thus possible to relate both the hardness and reduced modulus to the oxygen uptake (Fig. 5(c)). Two power law functions were used to identify the average elastic and hardness responses of the material as a function of the oxygen uptake. The identified equations are reported in Fig. 5(c) and recalled here:

$$E(\Delta[O]) = 125 + 5.0 * \Delta[O]^{0.65} \tag{11}$$

$$H(\Delta[O]) = 3.25 + 3.0 * \Delta[O]^{0.45} \tag{12}$$

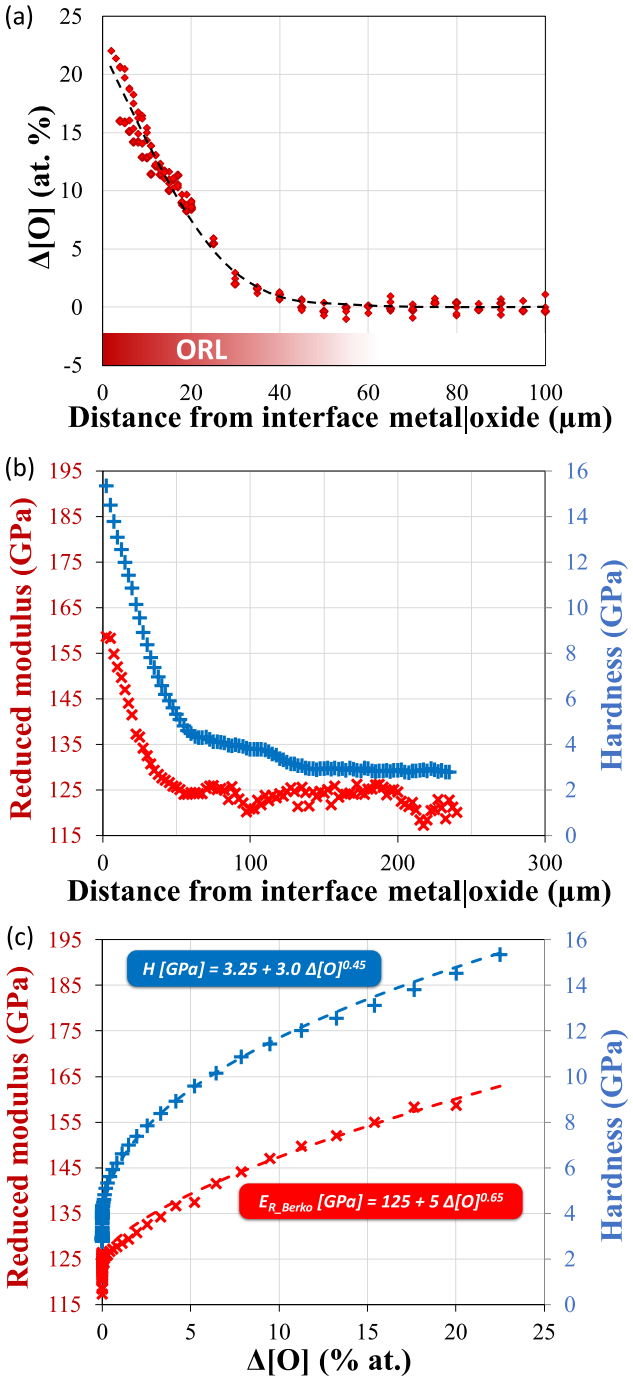

Figure 5: (a) EPMA profile as a function of the distance from the metal/oxide interface, (b) Hardness and reduced modulus average profile as a function of the distance from the metal/oxide interface, (c) Hardness and reduced modulus average profile as a function of the oxygen uptake.

3.3. Multi-modal characterization of the pre-oxidized material in the ORL

Based on the validation of the two previous investigations, the full-field analysis of both crystallographic and chemical content contributions to the local nanoindentation response appears feasible. A large HSNM map and EBSD

map were performed to cover both the ORL and the material non-affected by oxidation (Fig. 6(a) to (c)). EBSD map was also restricted to a scalar map corresponding to the declination angle °/, as shown in Fig. 6(d). Indents were visible using SEM and optical observations. Therefore, their position relative to the metal/oxide interface was known for all the indents, and subsequently the local oxygen uptake assuming that the oxygen front is flat and independent of the microstructure (Fig. 6(e) and (f)). It is worth noting that both the hardness and reduced modulus properties are affected by the oxygen uptake but also the crystal orientation, in the bulk and within the ORL.

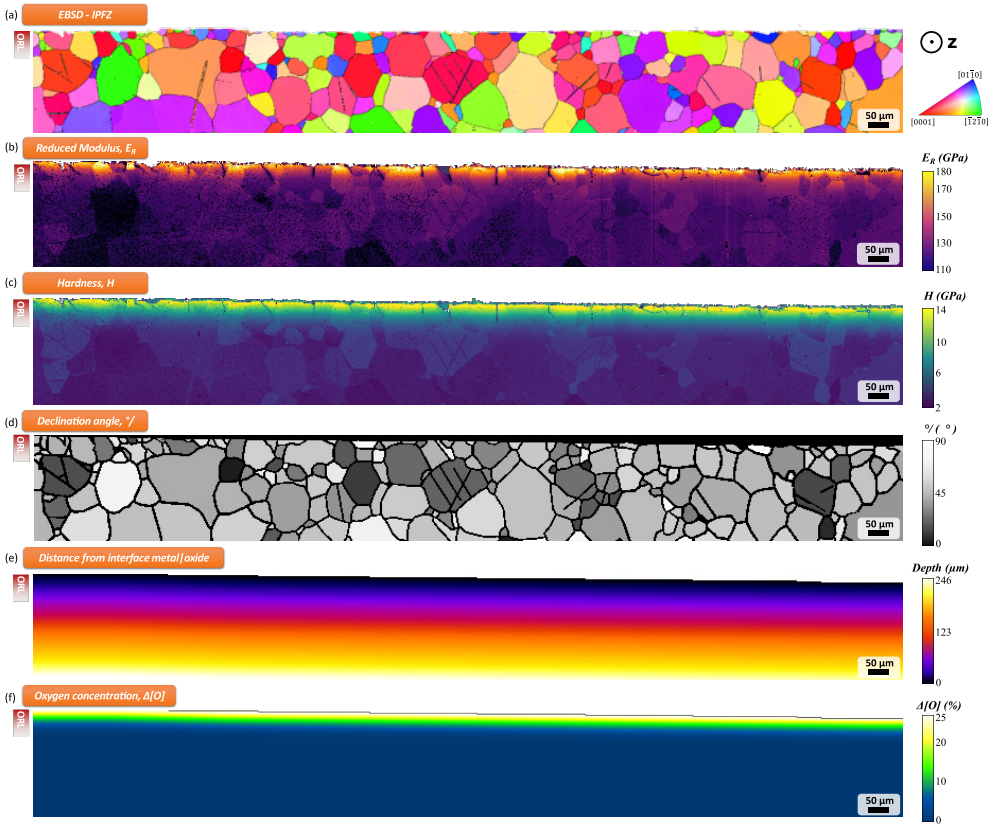

Figure 6: (a) Grain orientation map in reference to the LTD/Z direction for the pre-oxidized CP-Ti material, (b) Reduced modulus map using HSNM, (c) Hardness map using HSNM, (d) Declination (°/) map computed from EBSD measurements, (e) Map showing the distance of all the indents to the metal/oxide interface, (f) Calculated oxygen uptake map for all the indents.

As for the bulk material, data merging techniques were applied to the data of the pre-oxidized material in the ORL to relate hardness and reduced modulus properties to the oxygen uptake and crystal orientation (Fig. 7). The x-axis corresponds to the oxygen uptake while the color code corresponds to the declination angle, blue colors and red colors corresponding to low and high declination angles, respectively. An analytical solution has been suggested for both the reduced modulus and hardness as a function of the declination angle °/ and the oxygen uptake derived from the cos-form and the power law relationships with the declination angle and the oxygen uptake, respectively. Based on the increase in hardness and elastic anisotropy, a cross-term was added to account for interactions between oxygen uptake

and crystal orientation. Indeed, the difference in reduced modulus was 15 GPa for °/ ranging from 20 and 90° at 0 % oxygen uptake and 1.5 GPa for the difference in hardness. At 20 % oxygen uptake, the difference in reduced modulus and hardness was of 42 GPa and 4.1 GPa, respectively. The following expressions are suggested and reported as solid lines in Fig. 7:

$$E_{Berko}(\Delta[O],^{\circ}/) = 8.9cos(2^{\circ}/)(1 + 0.15\Delta[O]) + 125 + 9.0\Delta[O]^{0.65} \quad (13)$$

$$H(\Delta[O],^{\circ}/) = 0.68cos(2^{\circ}/)(1 + 0.17\Delta[O]) + 3.25 + 3.3\Delta[O]^{0.45} \quad (14)$$

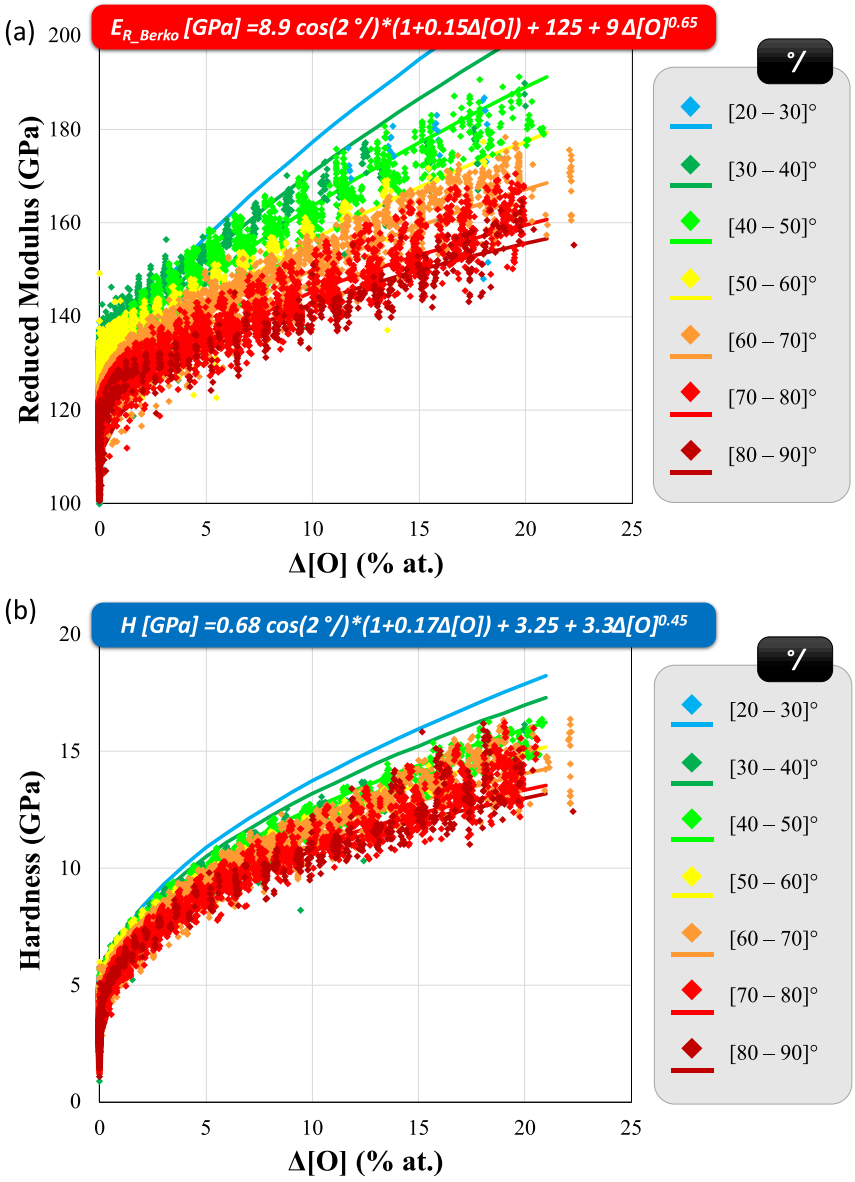

Figure 7: (a) Evolution of the reduced modulus as a function of the declination angle (color code) and the oxygen uptake, (b) Evolution of the hardness as a function of the declination angle (color code) and the oxygen uptake. Curves on identified equation were depicted as solid lines.

HSNM were conducted with a finer step size in the ORL (Fig. 8). Finer features such as twins were observed in this particular region but were not the purpose of the present paper. It is worth noting that some grains at the surface present a lower stiffness compared to the adjacent grains in depth due to crystallographic effect being stronger than the oxygen effect on the reduced modulus properties. This configuration is encountered when a $[01\bar{1}0]$- or a $[\bar{1}2\bar{1}0]$-oriented grain is closer to the surface compared to a [0001]-oriented grain. This case was less encountered for the hardness properties due to the significant variation of hardness properties with oxygen insertion. This specific configuration is highlighted with an arrow in Fig. 8. The evolution of the reduced modulus and hardness along this

arrow was illustrated in Fig. 9. An increase of 18 GPa in reduced modulus and 1.8 GPa in hardness was observed at the [01$\bar{1}$0]/[0001] grain boundary. Greater values of reduced modulus were found in the [0001] grain compared to the [01$\bar{1}$0] grain in the ORL.

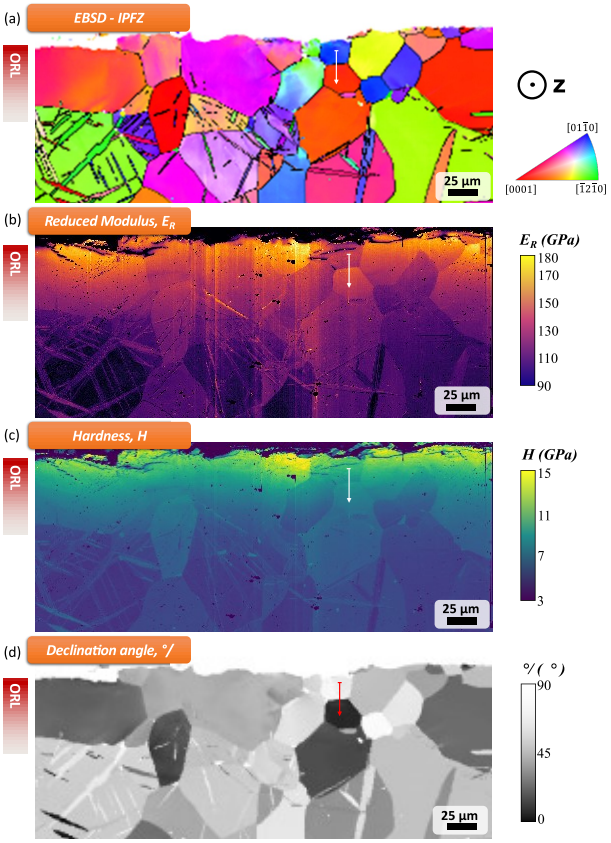

Figure 8: (a) Grain orientation map in reference to the LTD/Z direction for the pre-oxidized CP-Ti material, (b) Reduced modulus map using HSNM, (c) Hardness map using HSNM, (d) Declination (°/) map computed from EBSD measurements.

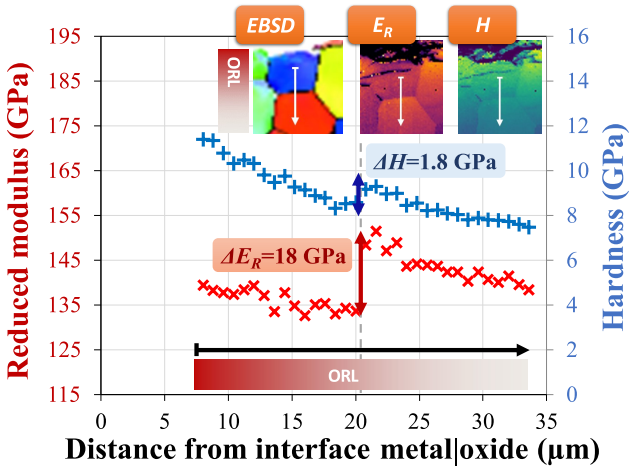

Figure 9: Evolution of the reduced modulus and hardness across a grain boundary from a [01$\bar{1}$0] to [0001] grain in the ORL.

3.4. Evolution of the elastic constants with the oxygen uptake

The reduced modulus is an apparent modulus for a multiaxial loading condition despite the directional application of the nanoindentation axis. Therefore, assessing the evolution of the elastic constants C_{ij} as a function of the oxygen uptake is more valuable since directly applicable to numerical simulations. The Vlassak and Nix theory was applied here to identify the evolution of the C_{ij} terms for different oxygen uptakes. Based on the previous identification of the reduced modulus evolution as a function of the oxygen content, power law relationships between C_{ij} terms and Δ[O] were imposed. Constants were selected so that the elastic constants at 0 % oxygen uptake, C_{ij} terms are equal to those previously used here and in the literature for CP-Ti material [42, 50]. The isotropy in the basal plane (transverse isotropy) was conserved regardless of the oxygen uptake, *i.e.*, C_{66}=0.5(C_{11}-C_{12}). A first minimization using a Nelder-Mead algorithm was tested with an exponent fixed at 0.65 for all the C_{ij} terms, similarly to the evolution of the reduced modulus as a function of the oxygen uptakes. Evolutions of the reduced modulus as with the oxygen uptake for extreme values of the declination angle made us decrease the exponent value of the C_{11} term and increase the one of the C_{33} term. A better identification was thus possible and the evolution of the identified reduced modulus from the experimental works (identification shown in Fig. 7) and the one simulated using the Vlassak and Nix theory are illustrated in Fig. 10(a) and (b) as a function of the oxygen uptake and the declination angle °/. Good agreement was found between the identified model and the experiments. The identified C_{ij} terms are reported below:

$$C_{11} = 162.2(1 + 0.0645\Delta[O]^{0.45}) \quad (15)$$

$$C_{12} = 91.8(1 + 0.04\Delta[O]^{0.65}) \quad (16)$$

$$C_{13} = 68.8(1 + 0.07\Delta[O]^{0.65}) \quad (17)$$

$$C_{33} = 180.5(1 + 0.055\Delta[O]^{0.9}) \quad (18)$$

$$C_{44} = 46.7(1 + 0.15\Delta[O]^{0.65}) \tag{19}$$

$$C_{66} = 0.5(C_{11} - C_{12}) \tag{20}$$

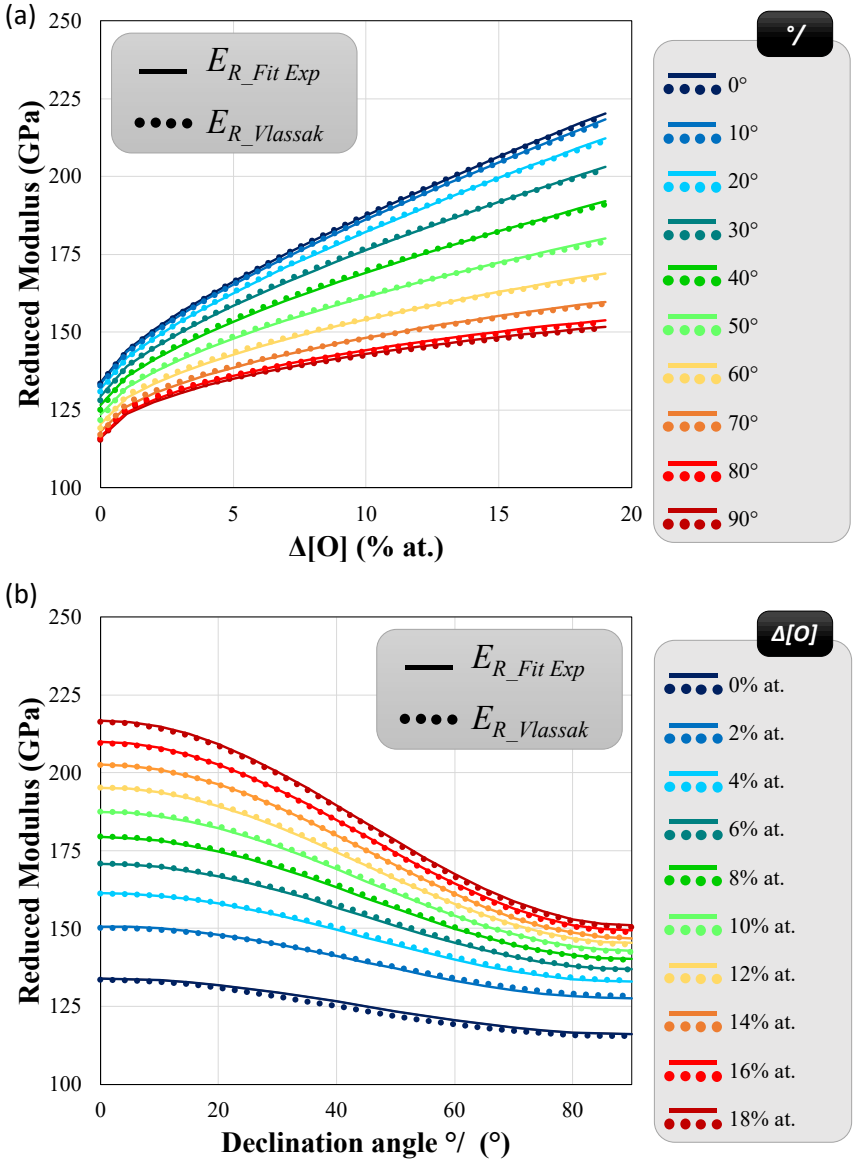

Figure 10: Evolution of the reduced modulus identified from the experimental values (solid lines) and from the Vlassak and Nix theory (dashed lines) as a function of the (a) oxygen uptake and (b) declination angle °/.

The C_{ij} terms for different oxygen uptakes were reported in Table. 3. The Young's modulus was also calculated for the $[01\bar{1}0]$ (a-axis) and the [0001] (c-axis) directions, corresponding to the softest and stiffest directions for hexagonal materials, respectively. In addition, the elastic anisotropy, considered as the ratio between $E_{[0001]}$ and $E_{[01\bar{1}0]}$, was computed and summarized in Table 3. For visual representation of the change in anisotropy of Ti due to oxygen

uptake, the evolution of the spatial dependence of Young's modulus in 3D of Ti with different oxygen uptakes was illustrated in Fig. 11 using a Python library [Github] developed by Kais AMMAR (*Centre des Matériaux, Mines Paris PSL*). The directional Young's modulus is represented to have the *c*-axis vertical and the basal plane in the center. Both the color code and morphology refer to the intensity of the spatial dependence of Young's modulus in 3D in spherical coordinates. The Young's modulus in 3D was represented for 0 %, 2 %, 5 %, 10 %, 15 %, and 20 % at. uptake of oxygen. Interestingly, the ovoid shape of the spatial dependence of Young's modulus in 3D progressively changed to a peanut shape function due to much stronger change in the C_{33} and C_{44} components. Indeed, C_{13}, C_{33} and C_{44} components increased by 49 %, 82 %, and 105 % for an oxygen uptake of 20 % at. while C_{11}, C_{12}, and C_{66} components increased by 25 %, 28 % and 21 %, respectively. $E_{[01\bar{1}0]}$ increased by 22 % while $E_{[0001]}$ increased by 83 % for an oxygen uptake of 20 % at.. In addition, the anisotropy was found to significantly increase with the oxygen uptake from 1.373 to 2.053 for an oxygen uptake of 0 and 20 %, respectively.

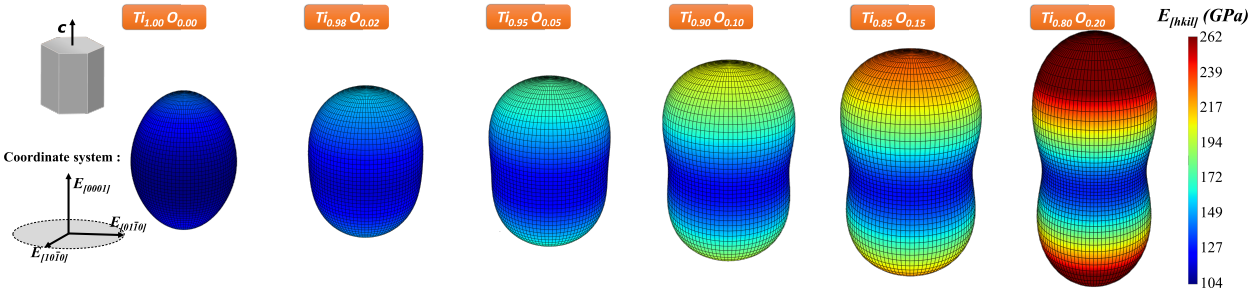

Figure 11: Evolution of the spatial dependence of Young's modulus in 3D of Ti with different oxygen uptakes: (a) 0 %, (b) 5 %, (c) 10 %, and (d) 15 %. Both size and color code indicate the intensity of the directional elastic modulus. The coordinate system illustrated on the bottom left represents a 100 GPa vector of Young's modulus along three directions of the hexagonal crystal structure.

4. Discussion

The present paper focuses on multi-modal characterization techniques to relate local mechanical properties assessed by high speed nanoindentation mapping (HSNM) to local chemical content and/or crystal orientation. The

Table 3: Evolution of the terms of the stiffness matrix for CP-titanium with oxygen uptake

Composition	C_{11} (GPa)	C_{12} (GPa)	C_{13} (GPa)	C_{33} (GPa)	C_{44} (GPa)	C_{66}	$E_{[01\bar{1}0]}$ (GPa)	$E_{[0001]}$ (GPa)	Anisotropy
$Ti_{100}O_0$	162.2	91.8	68.8	180.5	46.7	35.2	104.35	143.23	1.373
$Ti_{95}O_5$	183.8	102.3	82.5	222.8	66.6	40.8	119.66	175.22	1.464
$Ti_{90}O_{10}$	191.7	108.2	90.3	259.4	78.0	41.7	123.39	205.02	1.662
$Ti_{85}O_{15}$	197.6	113.1	96.8	294.1	87.4	42.2	125.81	233.78	1.858
$Ti_{80}O_{20}$	202.5	117.5	102.6	327.7	95.8	42.5	127.59	261.91	2.053

application case here was a CP-Ti material enriched or not by oxygen. Bulk CP-Ti was first chosen to solely investigate the role of crystallographic orientation on the hardness and elastic properties, for direct comparison with the extensive literature on this topic. It is worth mentioning that nanoindentation enforces multiaxial stress/strain fields beneath the indentor tip, at the difference of microtensile or micropillar compression techniques. Therefore, even if nanoindentation has the advantage to probe materials at a very local scale (here the microscale) such that properties can be considered uniform, a particular effort was done on the elastic properties to evaluate their directional fluctuations, *i.e.*, the stiffness matrix components C_{ij}, from inverse method using the Vlassak and Nix theory in anisotropic medium [62, 63, 69]. In addition, pre-oxidized CP-Ti material was used to concomitantly sound the effect of both the crystalline orientation and the local oxygen uptake within the ORL on the hardness and elastic properties (stiffness matrix components C_{ij}). To the authors' knowledge, such characterizations have not been reported in the literature. However, they are of prime importance for high-temperature structural applications using titanium that is subjected to oxidation.

HSNM technique is a recent characterization technique aiming at providing mechanical property images of heterogeneous materials with a nearly sub-micron spatial resolution [35, 59]. Such high resolution mapping requires small indent penetration depths with "indent spacing/penetration depth" ratio of at least 10. These techniques are particularly sensitive to surface preparation, determination of the contact point, resolution of the positioners and load cell, etc.. Therefore, a first demonstration of the technique was applied to the CP-Ti bulk material, a material extensively investigated in the literature using nanoindentation techniques [33, 35, 39, 41, 42] and can be considered here as our benchmark. This material, homogeneous in oxygen content in the bulk, is of interest in the presentation for direct comparison with the literature. Both the elastic properties and hardness are plotted in Fig. 12(a) and (b), respectively, and are compared with adapted references [33, 39, 41, 42].

For the elastic properties, the indentation modulus E_{Ind}, corrected by the 1.06 factor to account for the shape of the Berkovich tip [75], was plotted as a function of the declination angle. E_{Ind} data from Britton et al. [39] (Berkovich tip and Grade 1 CP-Ti) and Weaver et al. [42] (corrected spherical tip and Grade 1 CP-Ti) were added in Fig. 12(a). The present results (Berkovich tip and Grade 2 CP-Ti) are consistent with the literature, closer to Weaver et al.'s results than Britton et al.'s results. The latter results are slightly greater despite Grade 1 CP-Ti materials have a lower oxygen content than Grade 2 CP-Ti materials, oxygen having a stiffening effect. It is worth mentioning that despite the particular attention paid to the plane selection for larger representativity of declination angle, the present investigation is missing the 0 to 25° declination angle domain, for which the indentation modulus is maximal. Complementary angle domain can be obtained on the LTD-RD plane, but will be considered for further investigation. Despite the discrepancy in the results, the indentation modulus follows a cos-form evolution as a function of the declination angle. This trend matches particularly well with the identification of the indentation modulus with corrected spherical indentation using finite element calculations [42] or the Vlassak and Nix theory [62, 63, 69]. The discrepancy in results can arise from the non-consideration of the orientation of the Berkovich tip around the indentation axis while the spherical indentation might provide a unique result for a given declination angle. Therefore, a greater number of

grains and/or number of indents using Berkovich tip is needed to provide an average response for a given declination angle. In addition, some stress drops were observed during the CSM stabilized elastic modulus plateau due to plastic activity. These stress-drops affect the evaluation of the phase shift ϕ during CSM nanoindentation and subsequently the reduced modulus as a function of the penetration depth when stress-drops occur. Therefore, scatter observed within a grain can be partly explained by the number of stress-drops occurring in the fitted part of the reduced modulus as a function of the contact depth. Lower penetration and CSM amplitude lead to reduced scatter within a given grain, as depicted in Fig. 8 compared to Figs. 3 or 6. Fizanne-Michel et al. [41] have compared the elastic response of a Grade 2 CP-Ti material using either a Berkovich tip or a spherical tip. They did not find particular relation between the indentation modulus and the crystal orientation, regardless of the indentation tip. However, they found greater values of reduced modulus when using a spherical tip compared to a Berkovich tip. These results are different from the present findings and consideration for geometrical tip correction.

Similar comparison was done for the hardness, with data from Britton et al. [39] and Magazzeni et al. [33]. Despite slight change in Grade 1 and Grade 2 CP-Ti materials, the present results are consistent with Magazzeni et al.'s results. Greater hardness values were reported by Britton et al. despite lower oxygen content reported in the paper. Fizanne-Michel et al. [41] also investigated the evolution of hardness as a function of the crystal orientation using IPF representation. They found similar trends with $[01\bar{1}0]$ and $[2\bar{1}\bar{1}0]$ directions being the softest orientation while the [0001] direction is the hardest orientation. Reported hardness values ranged between 2.5 and 3.5 GPa when testing grains along directions from the $[01\bar{1}0]$ and $[2\bar{1}\bar{1}0]$ directions to the [0001] direction. These hardness values are consistent with the present study and Magazzeni et al.'s one. Hardness results reported by Britton et al. better match with a CP-Ti material with an oxygen uptake of 0.3 % using the relationship established in the present work linking the reduced modulus, the oxygen uptake and the declination angle (Fig. 12(b)).

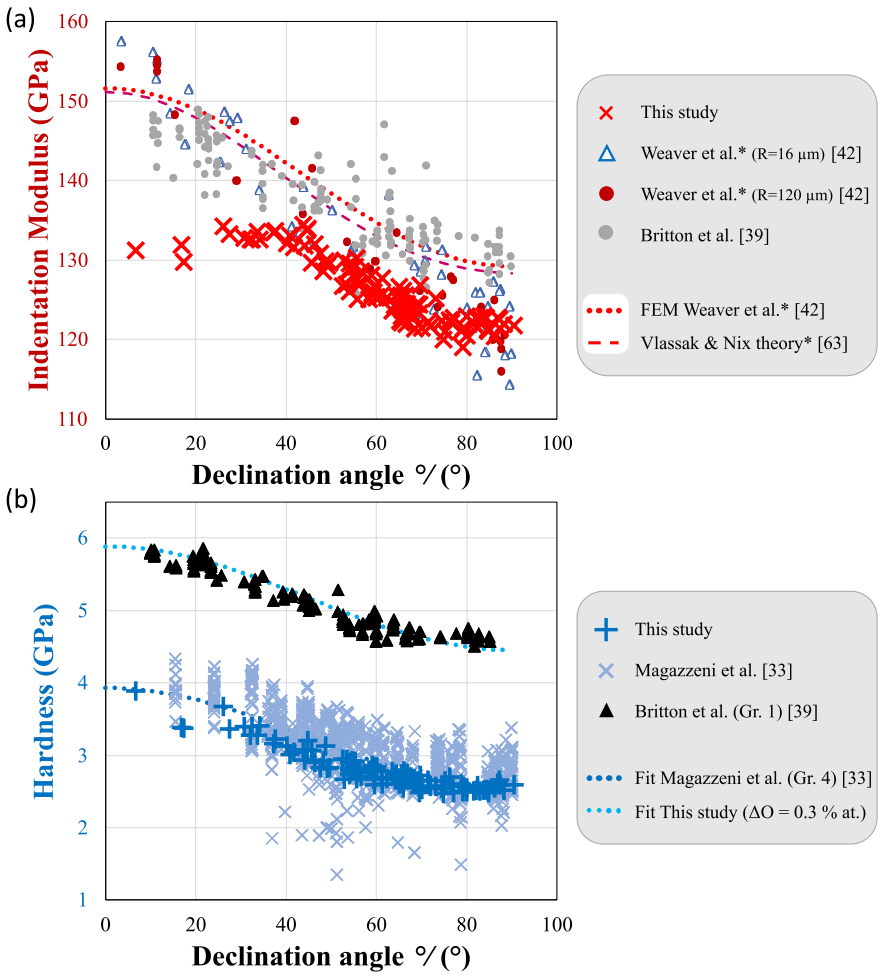

Figure 12: Evolution of the (a) indentation modulus and (b) hardness as a function of the declination angle $\sphericalangle$(°) compared with data and models from the literature. The asterisk corresponds to corrected values of reduced moduli considering the factor of 1.06, as was done by Aspinall et al. [75].

Based on these comparisons, the spatial resolution and the reproducibility of the results used in the present investigation demonstrate the feasibility of applying such a technique to chemical gradient-materials for high throughput multi-modal characterizations. Here, the final objective was to correlate nanoindentation properties to both crystal orientation and local oxygen concentration in a pre-oxidized CP-Ti material. Similar investigations were conducted by Magazenni et al. [33], solely focusing on the evolution of the hardness as a function of both the parameters. They also found a power law relationship between the hardness and the oxygen uptake (exponent of 0.6 compared to 0.45 in the present investigation). However, their limited number of tested orientations (nearly 10 grains) did not allow them to consider a cross-term between the declination angle and the oxygen uptake. Here, we have tested nearly 100 orientations within the ORL with greater range in declination angle. Therefore, we have considered a cross-term, since the difference in hardness along the soft and hard directions increases with the oxygen uptake (Fig. 7). In addition, a difference between both studies lays in the operating nanoindentation test, the present test being conducted under

displacement control while Magazzeni et al.'s tests were conducted under load control. For such mechanically-graded material, the indent size is consistent from indent to indent under displacement control but not under load control, indents being much smaller within the oxygen uptakes. This can also contribute to size effects on the obtained results due to difference in tested volume for indents with the oxygen-rich region and the bulk. One of the greater input of the paper was the capability to also probe the elastic response as a function of both the crystal orientation and the local oxygen uptake. To the best of the authors' knowledge, such multi-modal characterizations were done for the first time in the present paper. In the literature, the evolution of the elastic properties using experimental mean was only related to the oxygen uptake [10, 15, 27, 30, 34, 35, 46–48] but not to the declination angle. While the evolution of the reduced modulus (resp. indentation modulus) as a function of both the oxygen uptake and declination is an interesting input, it does not consider the multi-axiality of the loading inherent to the nanoindentation test. Therefore, numerical simulations using the Vlassak and Nix theory were used to directly relate the terms of the C_{ij} stiffness matrix as a function of the oxygen uptake. This high throughput characterization technique was thus capable to experimentally evaluate the evolution of the elastic anisotropy as a function of the oxygen uptake. Atomistic simulations were reported in the literature to numerically probe this change in anisotropy. Liang et al. [56] found similar evolution of C_{ij} terms with the oxygen uptake, C_{33} and C_{44} terms being the more sensitive to the oxygen uptake. They also found similar change from ovoid-shape to peanut-shape elastic 3D representation. The present correlative measurements and inverse method aim to experimentally confirm ab-initio calculations on this Ti-O system. The increase in elastic anisotropy and the much stiffer Young's modulus along the c-axis can arise from the anisotropic expansion of the crystal lattice due to oxygen insertion in the octahedral sites of the Ti lattice, the expansion being greater along the c-axis as reported by Cave et al. [78] and Baillieux et al. [79] using high energy diffraction techniques on pre-oxidized titanium specimens.

5. Conclusions

High speed nanoindentation mapping (HSNM) with micron- and sub-micron spatial resolution were performed to assess the local mechanical response of a CP-Ti material after 100 h pre-oxidation at 700 °C within the ORL and far from the ORL in the specimen bulk. Multi-modal correlative analyses were performed to relate nanoindentation properties, *i.e.*, reduced modulus and hardness, as a function of both the oxygen uptake and the declination angle (the angle between the indentation direction and the c-axis direction of the hexagonal crystal lattice). Cos-form and power law-form functions were found to describe well the fluctuations of nanoindentation properties with the declination angle and the oxygen uptake, respectively. Numerical simulations using the Vlassak and Nix theory brought a step further on the identification of elastic properties, providing the evolution of the C_{ij} terms of the stiffness matrix as a function of the oxygen uptake. Based on the stronger increase of the C_{33} and C_{44} terms with the oxygen uptake, the spatial dependence of Young's modulus in 3D changed from an ovoid-shape function to a peanut-shape-function as the anisotropy factor significantly increased with the oxygen uptake.

6. Author contribution

DT: Conceptualization, Methodology, Software, Validation, Formal Analysis, Investigation, Data curation, Writing, Visualization, Project Administration, Funding Acquisition.
TR: Conceptualization, Methodology, Software, Validation, Writing.
HP: Conceptualization, Writing.
AD: Formal Analysis, Investigation, Data curation.
QS: Methodology.
ML: Conceptualization, Supervision, Writing.

7. Data availability

The dataset for the bulk CP-Ti material will be shared as well as the Python code to register EBSD and nanoindentation data, to perform multimodal analyses, and to identify the C_{ij} terms using the Vlassak and Nix theory.

8. Acknowledgements

This work was supported by the European Research Council [project HT-S_4DefOx - Grant number 948007]. A [CC-BY public copyright license] has been applied by the authors to the present document and will be applied to all subsequent versions up to the Author Accepted Manuscript arising from this submission, in accordance with the grant's open access conditions. Henry Proudhon is thankful to the BIGMECA Chair for funding related work on the simulation of nanoindentation through the training of Emilie DESPINOY and allowing to start a collaboration with project HT-S_4DefOx. The authors warmly thank Roman MOUGINOT from FEMTOTOOLS(AG) for excellent technical and scientific supports. The authors are grateful to Kais AMMAR (Centre des Matériaux, Mines Paris PSL) for software development (Python) dedicated to the representation of the spatial dependence of Young's modulus in 3D. The authors thank Samuel FOREST for stimulating discussions and guidance. The authors particularly acknowledge the Raimond Castaing Microanalysis Centre (UAR 3623) for access to scanning electron microscopy access and microprobe analyses.

References

[1] M. Peters, J. Kumpfert, C. H. Ward, C. Leyens, Titanium alloys for aerospace applications, Advanced Engineering Materials 5 (2003) 419–427. doi:10.1002/adem.200310095.

[2] J. L. Murray, H. A. Wriedt, The O-Ti (Oxygen-Titanium) system, Journal of Phase Equilibria 8 (1987) 148–165. doi:10.1007/BF02873201.

[3] W. L. Finlay, J. A. Snyder, Effects of three interstitial solutes (nitrogen, oxygen, and carbon) on the mechanical properties of high-purity, alpha titanium, JOM 2 (1950) 277–286. doi:10.1007/BF03399001.

[4] P. Kofstad, P. B. Anderson, O. J. Krudtaa, Oxidation of titanium in the temperature range 800-1200°C, Journal of The Less-Common Metals 3 (1961) 89–97. doi:10.1016/0022-5088(61)90001-7.

[5] C. Dupressoire, A. Rouaix-Vande Put, P. Emile, C. Archambeau-Mirguet, R. Peraldi, D. Monceau, Effect of nitrogen on the kinetics of oxide scale growth and of oxygen dissolution in the Ti6242S titanium-based alloy, Oxidation of Metals 87 (2017) 343–353. doi:10.1007/s11085-017-9729-1.

[6] N. Vaché, D. Monceau, Oxygen Diffusion Modeling in Titanium Alloys: New Elements on the Analysis of Microhardness Profiles, Oxidation of Metals 93 (2020) 215–227. doi:10.1007/s11085-020-09956-9.

[7] C. Beevers, J. Robinson, Some observations on the influence of oxygen content on the fatigue behaviour of α-titanium, Journal of The Less-Common Metals 17 (1969) 345–352. doi:10.1016/0022-5088(69)90061-7.

[8] C. E. Shamblen, T. Redden, Air contamination and embrittlement of titanium alloys, in: The Science, Technology and Application of Titanium, London (UK), 1970, pp. 199–208. doi:10.1016/B978-0-08-006564-9.50027-0.

[9] G. Baur, P. Lehr, Influence spécifique de l'oxygène sur quelques propriétés physiques, les caractéristiques mécaniques et la dynamique de déformation plastique du titane de haute pureté, Journal of The Less-Common Metals 69 (1980) 203–218. doi:10.1016/0022-5088(80)90055-7.

[10] H. Conrad, Effect of interstitial solutes on the strength and ductility of titanium, Progress in Materials Science 26 (1981) 123–403. doi:https://doi.org/10.1016/0079-6425(81)90001-3.

[11] L. Bendersky, A. Rosen, The effect of exposure on the mechanical properties of the Ti-6Al-4v alloy, Engineering Fracture Mechanics 20 (1984) 303–311. doi:10.1016/0013-7944(84)90135-8.

[12] R. Shenoy, J. Unnam, R. Clark, Oxidation and embrittlement of Ti-6Al-2Sn-4Zr-2Mo alloy, Oxidation of Metals 26 (1986) 105–124. doi:10.1007/BF00664276.

[13] M. Wasz, F. Brotzen, R. McLellan, A. Griffin, Effect of oxygen and hydrogen on mechanical properties of commercial purity titanium, International Materials Reviews 41 (1996) 1–12. doi:10.1179/imr.1996.41.1.1.

[14] T. A. Parthasarathy, W. J. Porter, S. Boone, R. John, P. Martin, Life prediction under tension of titanium alloys that develop an oxygenated brittle case during use, Scripta Materialia 65 (2011) 420–423. doi:https://doi.org/10.1016/j.scriptamat.2011.05.025.

[15] M. C. Brandes, M. Baughman, M. J. Mills, J. C. Williams, The effect of oxygen and stress state on the yield behavior of commercially pure titanium, Materials Science and Engineering A 551 (2012) 13–18. doi:10.1016/j.msea.2012.04.058.

[16] M. Yan, W. Xu, M. S. Dargusch, H. P. Tang, M. Brandt, M. Qian, Review of effect of oxygen on room temperature ductility of titanium and titanium alloys, Powder Metallurgy 57 (2014) 251–257. URL: https://doi.org/10.1179/1743290114Y.0000000108. doi:10.1179/1743290114Y.0000000108.

[17] H. Hornberger, C. Randow, C. Fleck, Fatigue and surface structure of titanium after oxygen diffusion hardening, Materials Science and Engineering A 630 (2015) 51–57. doi:10.1016/j.msea.2015.02.006.

[18] A. A. Hidalgo, T. Ebel, W. Limberg, F. Pyczak, Influence of oxygen on the fatigue behaviour of Ti-6Al-7Nb alloy, Key Engineering Materials 704 (2016) 44–52. doi:10.4028/www.scientific.net/KEM.704.44.

[19] D. Satko, J. Shaffer, J. Tiley, S. Semiatin, A. Pilchak, S. Kalidindi, Y. Kosaka, M. Glavicic, A. Salem, Effect of microstructure on oxygen rich layer evolution and its impact on fatigue life during high-temperature application of α/β titanium, Acta Materialia 107 (2016) 377–389. doi:10.1016/j.actamat.2016.01.058.

[20] J. Q. Ren, Q. Wang, X. F. Lu, W. F. Liu, P. L. Zhang, X. B. Zhang, Effect of oxygen content on active deformation systems in pure titanium polycrystals, Materials Science and Engineering A 731 (2018) 530–538. doi:10.1016/j.msea.2018.06.083.

[21] D. Texier, Q. Sirvin, V. Velay, M. Salem, D. Monceau, B. Mazères, E. Andrieu, R. Roumiguier, B. Dod, Oxygen / nitrogen-assisted embrittlement of titanium alloys exposed at elevated temperature, MATEC Web Conf. 321 (2020) 06004. doi:10.1051/matecconf/202032106004.

[22] A. Casadebaigt, J. Hugues, D. Monceau, High temperature oxidation and embrittlement at 500–600 °C of Ti-6Al-4V alloy fabricated by Laser and Electron Beam Melting, Corrosion Science 175 (2020) 108875. doi:10.1016/j.corsci.2020.108875.

[23] Q. Sirvin, D. Texier, J. Genée, V. Velay, D. Monceau, B. Dod, Oxygen content effect on mechanical behavior of CP titanium exposed at elevated temperature, in: Titanium 2023, Edimbourg, 2023.

[24] A. Amherd Hidalgo, T. Ebel, R. Frykholm, E. Carreño-Morelli, F. Pyczak, High-oxygen MIM Ti-6Al-7Nb: Microstructure, tensile and fatigue properties, Materials Today Communications 34 (2023). doi:10.1016/j.mtcomm.2022.104982.

[25] X.-Q. Wang, W.-Z. Han, Oxygen-gradient titanium with high strength, strain hardening and toughness, Acta Materialia 246 (2023) 118674. doi:https://doi.org/10.1016/j.actamat.2023.118674.

[26] F. Amann, R. Poulain, S. Delannoy, J. Couzinié, E. Clouet, I. Guillot, F. Prima, An improved combination of tensile strength and ductility in titanium alloys via oxygen ordering, Materials Science and Engineering: A 867 (2023) 144720. doi:https://doi.org/10.1016/j.msea.2023.144720.

[27] D. Texier, A. Palchoudhary, J. Genée, Q. Sirvin, Y. Zhang, G. Kermouche, D. Monceau, D. Poquillon, E. Andrieu, Effect of oxygen dissolution on the mechanical behavior of thin Ti-6Al-4V specimens oxidized at high temperature: Experimental and modelling approach, Corrosion Science 235 (2024) 112177. doi:https://doi.org/10.1016/j.corsci.2024.112177.

[28] B. Barkia, V. Doquet, J. P. Couzinié, I. Guillot, E. Héripré, In situ monitoring of the deformation mechanisms in titanium with different oxygen contents, Materials Science and Engineering A 636 (2015) 91–102. doi:10.1016/j.msea.2015.03.044.

[29] J.-P. Couzinie, B. Barkia, V. Doquet, I. Guillot, Influence of hydrogen and oxygen content on the mechanical behavior of zirconium between 275 and 325°C and titanium at 20°C, in: 2012 International hydrogen conference, Jakson Lake (USA), 2014, pp. 411–419.

[30] F. B. Vicente, D. R. N. Correa, T. A. G. Donato, V. E. Arana-Chavez, M. A. R. Buzalaf, C. R. Grandini, The influence of small quantities of oxygen in the structure, microstructure, hardness, elasticity modulus and cytocompatibility of Ti-Zr alloys for dental applications, Materials 7 (2014) 542–553. doi:10.3390/ma7010542.

[31] Y. Chong, M. Poschmann, R. Zhang, S. Zhao, M. S. Hooshmand, E. Rothchild, D. L. Olmsted, J. W. Morris, D. C. Chrzan, M. Asta, A. M. Minor, Mechanistic basis of oxygen sensitivity in titanium, Science Advances 6 (2020) eabc4060. doi:10.1126/sciadv.abc4060.

[32] J. Oh, B. Lee, S.-W. Cho, S.-W. Lee, G.-S. Choi, J.-W. Lim, Oxygen effects on the mechanical properties and lattice strain of Ti and Ti-6Al-4V, Metals and Materials International 17 (2011) 733–736. doi:10.1007/s12540-011-1006-2.

[33] C. M. Magazzeni, H. M. Gardner, I. Howe, P. Gopon, J. C. Waite, D. Rugg, D. E. Armstrong, A. J. Wilkinson, Nanoindentation in multi-modal map combinations: a correlative approach to local mechanical property assessment, Journal of Materials Research 36 (2021) 2235–2250. doi:10.1557/s43578-020-00035-y.

[34] Z. Cai, T. Xiang, W. Bao, J. Chen, T. Gao, G. Xie, Enhancing strength and ductility of pure titanium by interstitial oxygen atoms, Materials Science, SSRN Electronic Journal 14 (2022).

[35] D. Texier, Q. Sirvin, A. Dziri, H. Proudhon, V. Yastrebov, M. Legros, Effect of oxygen content on the sub-grain nanoindentation response in titanium affected by high temperature oxidation, in: Titanium 2023, Edimbourg, 2023.

[36] F. Kværndrup, Ö. Kücükyildiz, G. Winther, M. Somers, T. Christiansen, Extreme hardening of titanium with colossal interstitial contents of nitrogen and oxygen, Materials Science and Engineering A 813 (2021) 141033. doi:10.1016/j.msea.2021.141033.

[37] C. J. Rosa, Oxygen diffusion in alpha and beta titanium in the temperature range of 932° to 1142°C, Metallurgical Transactions 1 (1970) 2517–2522. doi:10.1007/978-3-319-45713-0_10.

[38] G. B. Viswanathan, E. Lee, D. M. Maher, S. Banerjee, H. L. Fraser, Direct observations and analyses of dislocation substructures in the α phase of an α/β Ti-alloy formed by nanoindentation, Acta Materialia 53 (2005) 5101–5115. doi:10.1016/j.actamat.2005.07.030.

[39] T. Britton, H. Liang, F. Dunne, A. Wilkinson, The effect of crystal orientation on the indentation response of commercially pure titanium:

experiments and simulations, in: Proc. R. Soc. A., Jakson Lake (USA), 2010, pp. 466695—-719. doi:http://doi.org/10.1098/rspa.2009.0455.

[40] C. Zambaldi, Y. Yang, T. R. Bieler, D. Raabe, Orientation informed nanoindentation of α-titanium: Indentation pileup in hexagonal metals deforming by prismatic slip, Journal of Materials Research 27 (2012) 356–367. doi:10.1557/jmr.2011.334.

[41] C. Fizanne-Michel, M. Cornen, P. Castany, I. Péron, T. Gloriant, Determination of hardness and elastic modulus inverse pole figures of a polycrystalline commercially pure titanium by coupling nanoindentation and EBSD techniques, Materials Science and Engineering: A 613 (2014) 159–162. doi:10.1016/j.msea.2014.06.098.

[42] J. Weaver, M. Priddy, D. McDowell, S. Kalidindi, On capturing the grain-scale elastic and plastic anisotropy of alpha-Ti with spherical nanoindentation and electron back-scattered diffraction, Acta Materialia 117 (2016) 23–34. doi:10.1016/j.actamat.2016.06.053.

[43] M. Kalyan Phani, A. Kumar, W. Arnold, K. Samwer, Elastic stiffness and damping measurements in titanium alloys using atomic force acoustic microscopy, Journal of Alloys and Compounds 676 (2016) 397–406. doi:10.1016/j.jallcom.2016.03.155.

[44] Z. Liu, J. Zhang, B. He, Y. Zou, High-speed nanoindentation mapping of a near-alpha titanium alloy made by additive manufacturing, Journal of Materials Research 36 (2021) 2223–2234. doi:10.1557/s43578-021-00204-7.

[45] Z. Liu, L. Lang, S. M. Mohammed, D. Chen, B. He, Y. Zou, Small-depth nanoindentation studies of an additively manufactured titanium alloy: Anisotropic nanomechanical properties and correlation with microscopic mechanical behaviour, Materialia 30 (2023) 101802. doi:10.1016/j.mtla.2023.101802.

[46] Y. Lee, G. Welsch, Young's modulus and damping of Ti6Al4V alloy as a function of heat treatment and oxygen concentration, Materials Science and Engineering A 128 (1990) 77–89. doi:10.1016/0921-5093(90)90097-M.

[47] P. Kwasniak, M. Muzyk, H. Garbacz, K. Kurzydlowski, Influence of oxygen content on the mechanical properties of hexagonal Ti-First principles calculations, Materials Science and Engineering A 590 (2014) 74–79. doi:10.1016/j.msea.2013.10.004.

[48] J. Baillieux, C. Archambeau, P. Emile, D. Poquillon, Effet de la diffusion de l'oxygène sur le comportement mécanique du Ti–6Al–2Sn–4Zr–2Mo–0.1Si, in: CFM2015, Lyon (France), 2015, pp. 22–25.

[49] E. Fisher, C. Renken, Single-crystal elastic moduli and the hcp → bcc transformation in Ti, Zr, and Hf, Physical Review 135 (1964) 482–494. doi:10.1103/PhysRev.135.A482.

[50] G. Simmons, H. Wang, Single crystal elastic constants and calculated aggregate properties: A handbook, M.I.T. Press, Cambridge, Mass, 1971.

[51] R. Hearmon, The elastic constants of crystals and other anisotropic materials, Springer-Verlag, Berlin, 1979.

[52] F. Bridier, D. L. McDowell, P. Villechaise, J. Mendez, Crystal plasticity modeling of slip activity in Ti-6Al-4V under high cycle fatigue loading, International Journal of Plasticity 25 (2009) 1066–1082. doi:10.1016/j.ijplas.2008.08.004.

[53] D. Tromans, Elastic anisotropy of HCP metal crystals and polycrystals, Ijrras 6 (2011) 462–483.

[54] L. Yin, O. Umezawa, Heterogeneous deformation in a commercially pure titanium sheet under dwell fatigue loading: crystal plasticity modeling and experiment, ISIJ International 61 (2021) 1990–2001. doi:10.2355/isijinternational.ISIJINT-2020-702.

[55] E. Emelianova, V. Romanova, R. Balokhonov, M. Pisarev, O. Zinovieva, A numerical study of the contribution of different slip systems to the deformation response of polycrystalline titanium, Physical Mesomechanics 24 (2021) 166–177. doi:https://doi.org/10.1134/S1029959921020065.

[56] L. Liang, Simulation ab initio des défauts étendus du Ti en présence d'interstitiels H et O, Ph.D. thesis, 2016. URL: http://www.theses.fr/2016SACLX009/document.

[57] H. Besharatloo, J. M. Wheeler, Influence of indentation size and spacing on statistical phase analysis via high-speed nanoindentation mapping of metal alloys, Journal of Materials Research 36 (2021) 2198–2212. doi:10.1557/s43578-021-00214-5.

[58] J. Wheeler, B. Gan, R. Spolenak, Combinatorial investigation of the Ni–Ta system via correlated high-speed nanoindentation and EDX mapping, Small Methods 6 (2022) 1–6. doi:10.1002/smtd.202101084.

[59] E. Rossi, J. Wheeler, M. Sebastiani, High-speed nanoindentation mapping: A review of recent advances and applications, Current Opinion in Solid State and Materials Science 27 (2023) 101107. doi:10.1016/j.cossms.2023.101107.

[60] M. Seehaus, S. H. Lee, T. Stollenwerk, J. M. Wheeler, S. Korte-Kerzel, Estimation of directional single crystal elastic properties from nanoindentation by correlation with EBSD and first-principle calculations, Materials and Design 234 (2023) 112296. doi:10.1016/j.matdes.2023.112296.

[61] E. Herbert, W. Oliver, G. Pharr, Nanoindentation and the dynamic characterization of viscoelastic solids, Journal of Physics D: Applied Physics 41 (2008). doi:10.1088/0022-3727/41/7/074021.

[62] J. Vlassak, W. Nix, Measuring the elastic properties of anisotropic materials by means of indentation experiments, Journal of the Mechanics and Physics of Solids 42 (1994) 1223–1245. doi:10.1016/0022-5096(94)90033-7.

[63] J. Vlassak, M. Ciavarella, J. Barber, X. Wang, The indentation modulus of elastically anisotropic materials for indenters of arbitrary shape, Journal of the Mechanics and Physics of Solids 51 (2003) 1701–1721. doi:10.1016/S0022-5096(03)00066-8.

[64] D. Texier, D. Monceau, J.-C. Salabura, R. Mainguy, E. Andrieu, Micromechanical testing of ultrathin layered material specimens at elevated temperature, Materials at high temperatures 33 (2016) 325–337. doi:10.1080/09603409.2016.1182250.

[65] R. Hielscher, H. Schaeben, A novel pole figure inversion method: Specification of the MTEX algorithm, Journal of Applied Crystallography 41 (2008) 1024–1037. doi:10.1107/S0021889808030112.

[66] A. Marano, C. Ribart, H. Proudhon, Towards a data platform for multimodal 4d mechanics of material microstructures, Current Opinion in Solid State and Materials Science submitted (2024). URL: https://github.com/heprom/pymicro.

[67] I. N. Sneddon, The relation between load and penetration in the axisymmetric boussinesq problem for a punch of arbitrary profile, International Journal of Engineering Science 3 (1965) 47–57. doi:https://doi.org/10.1016/0020-7225(65)90019-4.

[68] R. King, Elastic analysis of some punch problems for a layered medium, International Journal of Solids and Structures 23 (1987) 1657–1664. doi:10.1016/0020-7683(87)90116-8.

[69] J. J. Vlassak, W. Nix, Indentation modulus of elastically anisotropic half spaces, Philosophical Magazine A 67 (1993) 1045–1056.

[70] D. Barnett, J. Lothe, Line force loadings on anisotropic half-spaces and wedges, Physica Norvegica 8 (1975) 13–22.

[71] A. Stroh, Dislocations and cracks in anisotropic elasticity, Philosophical magazine 3 (1958) 625–646.

[72] D. Bacon, D. Barnett, R. O. Scattergood, Anisotropic continuum theory of lattice defects, Progress in Materials Science 23 (1980) 51–262.

[73] T. Ting, Image singularities of green's functions for anisotropic elastic half-spaces and bimaterials, The Quarterly Journal of Mechanics and Applied Mathematics 45 (1992) 119–139.

[74] J. Yin, D. M. Barnett, W. Cai, Efficient computation of forces on dislocation segments in anisotropic elasticity, Modelling and Simulation in Materials Science and Engineering 18 (2010) 045013.

[75] J. Aspinall, D. Armstrong, M. Pasta, EBSD-coupled indentation: nanoscale mechanics of lithium metal, Materials Today Energy 30 (2022) 101183. doi:10.1016/j.mtener.2022.101183.

[76] H. Proudhon, T. Richeton, D. Texier, A. Dziri, Q. Sirvin, M. Legros, Correlative analysis of EBSD and high speed nanoindentation mapping datasets in pure titanium, 2024. doi:10.5281/zenodo.10842559.

[77] A. Fick, Ueber Diffusion, Annalen der Physik 170 (1855) 59–86. doi:https://doi.org/10.1002/andp.18551700105.

[78] K. Cavé, D. Texier, S. Vallot, N. Chanfreau, E. Fessler, M. Dehmas, D. Monceau, D. Poquillon, Effect of creep loading on the oxygen diffusion of Ti6242S at 650 °C, Scripta Materialia (2023) submitted.

[79] D. P. J. Baillieux, B. Malard, Observation using synchrotron x-ray diffraction of the crystallographic evolution of α-titanium after oxygen diffusion, Philosophical Magazine Letters 95 (2015) 245–252. doi:10.1080/09500839.2015.1014876.

Appendix 1: Literature review of C_{ij} terms of the stiffness matrix used for pure titanium and some alloys

The elastic anisotropy of CP-Ti materials has been investigated using different techniques. Different sets of C_{ij} terms of the stiffness matrix were reported in the literature, either from handbooks, citations, experiments or simulations. Sets of C_{ij} terms of the stiffness matrix for CP-Ti are summarized in Table A1. For comparison purpose (finite element model versus Vlassak and Nix theory) and similarities between sets of C_{ij} terms, those used in Refs. [42] will be considered here for the bulk CP-Ti.

Table 4: Terms of the stiffness matrix for CP-titanium

C_{11} (GPa)	C_{12} (GPa)	C_{13} (GPa)	C_{33} (GPa)	C_{44} (GPa)	C_{66} (GPa)	Ref.
162.4	92.0	69.0	180.7	49.7	35.2	[50, 52] from [50]
162.2	91.8	68.8	180.5	46.7	35.2	[42] from [50]
162.4	92.0	69.0	180.7	49.7	76.5[2]	[40] from [50]
162.4	92.0	69.0	180.7	46.7	35.2	[49, 54] from [49]
160.0	90.0	66.0	181.0	46.5	35.0	[53] from [51]
162.0	92.0	69.0	181.0	47.0	34.0	[55] from [55]
162.4	92.0	69.0	180.7	117.0	35.2	[39] from [38]
186.0	88.0	84.0	191.0	47.0	49.0	[56]

Liang et al. [56] have performed atomistic simulations to identify the C_{ij} terms of the stiffness matrix for titanium material with different concentrations of oxygen.

Table 5: Terms of the stiffness matrix for CP-titanium with different oxygen concentrations from [56]

Composition	C_{11} (GPa)	C_{12} (GPa)	C_{13} (GPa)	C_{33} (GPa)	C_{44} (GPa)	C_{66} (GPa)
$Ti_{100.0}O_{0.0}$	186.0	88.0	84.0	191.0	47.0	49.0
$Ti_{99.0}O_{1.0}$	186.0	95.0	83.0	207.0	47.0	45.0
$Ti_{97.3}O_{2.7}$	207.0	106.0	81.0	228.0	56.0	51.0
$Ti_{94.1}O_{5.9}$	201.0	115.0	86.0	230.0	57.0	43.0
$Ti_{88.9}O_{11.1}$	245.0	170.0	96.0	244.0	71.0	64.0
$Ti_{80.0}O_{20.0}$	227.0	164.0	111.0	300.0	84.0	31.0

[2]This value is about 2 times C_{66}

Appendix 2: CSM methodology and Berkovich tip calibration

Additional information are detailed in this Appendix for reading convenience. Unlike conventional nanoindentation, the continuous stiffness measurement (CSM) technique allows elastic and hardness properties to be probed throughout the loading phase applying a sin-form stimulation during the loading phase. A schematic illustration of the CSM nanoindentation test showing the sin/cos-form input and output signals during the loading condition is shown in Fig. 13. CSM tests can be conducted under either force-controlled mode, position-controlled mode, or displacement-controlled mode. Each controlled mode has its advantages and drawbacks. Load-controlled and position-controlled modes are easier to be performed due to direct measurement of load and sensor position using optical encoders. Tests under displacement-controlled mode consider correction of the position based on the compliance of the sensing module and is thus related to both position and load. However, this measurement mode is particularly relevant to probe material with gradient of mechanical properties since it maintains similar indentation depths from indent to indent regardless of the local mechanical response. Conversely, indentation depths are different when carrying out experiments under load-controlled and position-controlled modes. It is worth mentioning that materials might be sensitive to indentation size effects and thus, to the indentation control mode. In this study, CSM tests were performed under displacement-controlled mode due to the severe gradient of mechanical properties expected within the ORL. Different frequencies have to be considered for this dynamic test, *i.e.*, the CSM frequency f_{CSM}, the testing frequency f_{test}, and the acquisition frequency $f_{acquis.}$. The CSM frequency f_{CSM} corresponds to the frequency of the sin/cos-form signal added to the displacement during the tip actuation. The CSM frequency is here equal to 200 Hz. The testing frequency f_{test} corresponds to the frequency of data collection for the control and regulation of the nanoindentation testing device and is equal to 94 kHz. Displacement, positions, load, moving average of the phase shift Φ_n, etc., were collected at this high frequency but saved for the determination of hardness H and reduced modulus E_R at the acquisition frequency $f_{acquis.}$ between 50 and 400 Hz.

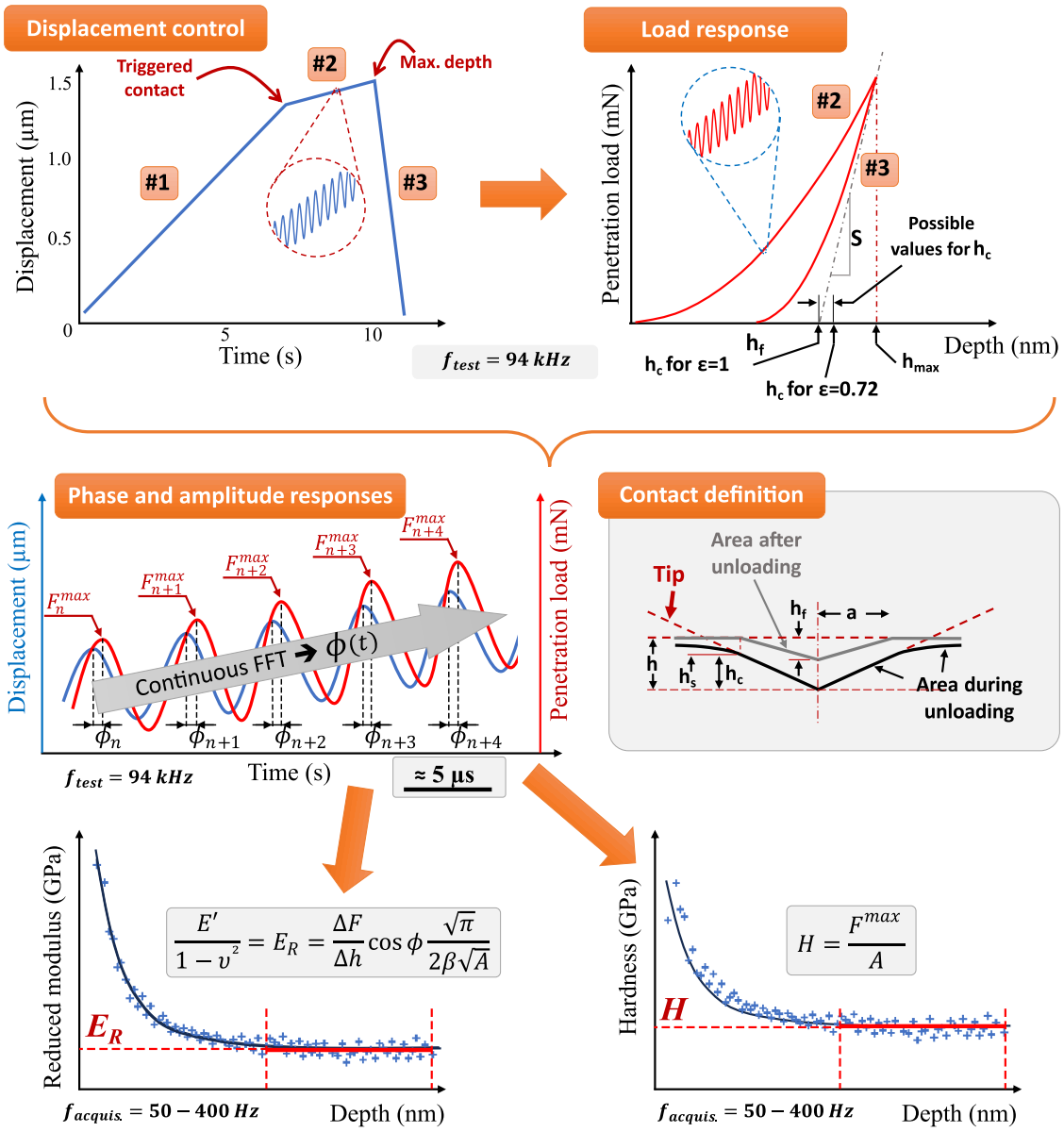

Figure 13: Schematic illustration of the indentation testing in CSM mode. Imposed displacement and penetration response as a function of time. Magnified region of the displacement/penetration load signal showing the phase shift used for the identification of the reduced modulus (E_R) and the hardness (H). Definition of the contact parameters. Stabilized E_R and H as a function of the contact depth.

As described in the manuscript, the calibration of the diamond Berkovich tip was performed on fused silica. Based on the stabilized values of the reduced modulus E_R (E_R of 69.6 GPa for the fused silica with a diamond tip) and hardness H (H of 9.4 GPa for the fused silica) as a function of the contact depth. Calibration tests were carried out using CSM technique in displacement-controlled mode. The calibration results on fused silica are depicted in Fig. 14 and the hardness and reduced modulus values were stabilized between 20 and 160 nm.

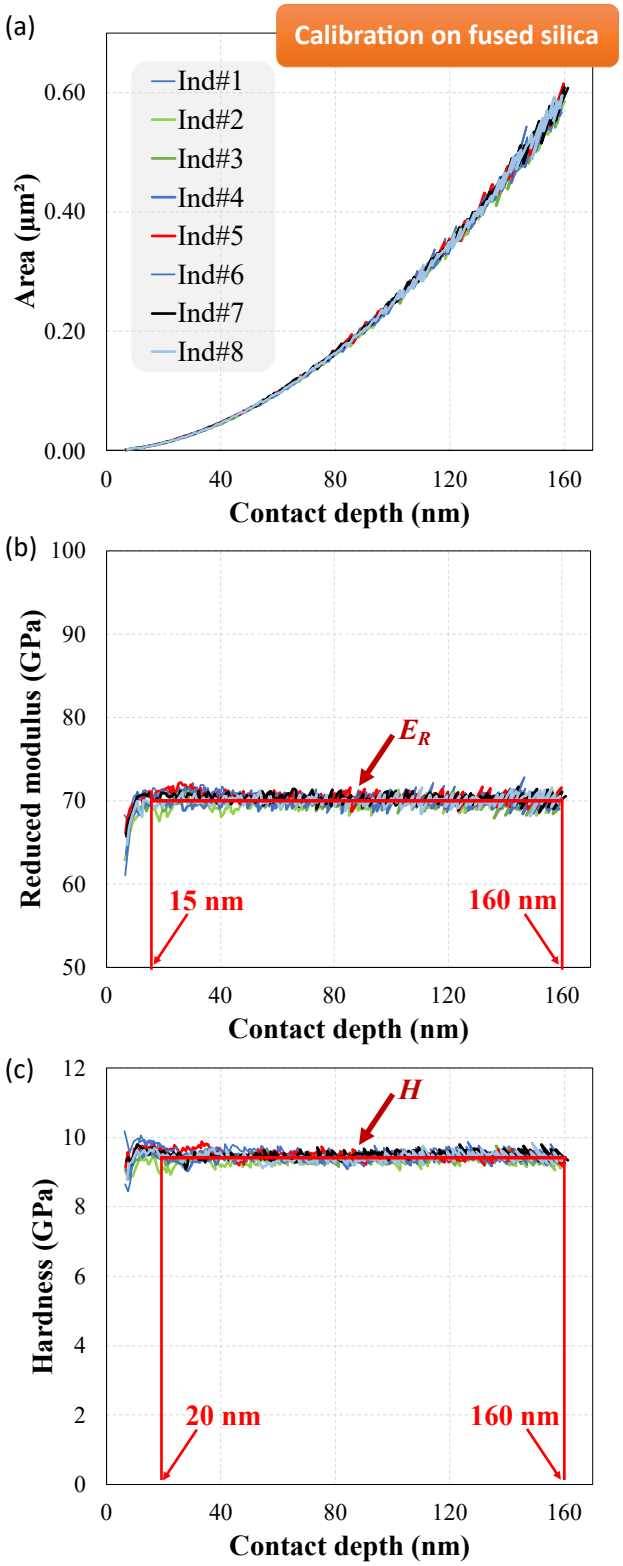

Figure 14: Evolution of : (a) the contact area as a function of the penetration depth, (b) the Reduced modulus as a function of the penetration depth, (c) the Hardness as a function of the penetration depth.